ISLAND: INFORMING BRIGHTNESS AND SURFACE TEMPERATURE THROUGH A LAND COVER-BASED INTERPOLATOR

A PREPRINT

Yuhao Liu
Rice University
yuhao.liu@rice.edu

Pranavesh Panakkal
Rice University
pranavesh@rice.edu

Sylvia Dee
Rice University
sylvia.dee@rice.edu

Guha Balakrishnan
Rice University
guha@rice.edu

Jamie Padgett
Rice University
jamie.padgett@rice.edu

Ashok Veeraraghavan *
Rice University
vashok@rice.edu

ABSTRACT

Cloud occlusion is a common problem in the field of remote sensing, particularly for thermal infrared imaging. Remote sensing thermal instruments onboard operational satellites are supposed to enable frequent and high-resolution observations over land; unfortunately, clouds adversely affect thermal signals by blocking outgoing longwave radiation emission from Earth's surface, interfering with the retrieved ground emission temperature. Such cloud contamination severely reduces the set of serviceable thermal images for downstream applications, making it impractical to perform intricate time-series analysis of land surface temperature (LST). In this paper, we introduce a novel method to remove cloud occlusions from Landsat 8 LST images. We call our method ISLAND, an acronym for Informing Brightness and Surface Temperature Through a Land Cover-based Interpolator. Our approach uses thermal infrared images from Landsat 8 (at 30 m resolution with 16-day revisit cycles) and the NLCD land cover dataset. Inspired by Tobler's first law of Geography, ISLAND predicts occluded brightness temperature and LST through a set of spatio-temporal filters that perform distance-weighted spatio-temporal interpolation. A critical feature of ISLAND is that the filters are land cover-class aware, making it particularly advantageous in complex urban settings with heterogeneous land cover types and distributions. Through qualitative and quantitative analysis, we show that ISLAND achieves robust reconstruction performance across a variety of cloud occlusion and surface land cover conditions, and with a high spatio-temporal resolution. We provide a public dataset of 20 U.S. cities with pre-computed ISLAND thermal infrared and LST outputs. Using several case studies, we demonstrate that ISLAND opens the door to a multitude of high-impact urban and environmental applications across the continental United States.

Keywords cloud removal · land surface temperature · thermal imaging · Landsat · land cover

1 Introduction

Land surface temperature (LST) is a fundamental aspect of Earth's climate system, it attracts extensive studies across diverse disciplines. The wide array of fields include climate change [Horton et al., 2016, Seneviratne et al., 2021], urban planning [Sobrino et al., 2013, Huang and Wang, 2019], vegetation and land cover changes [Gomez-Martinez et al., 2021], and human health [Orimoloye et al., 2018, Dee et al., 2022]. LST changes rapidly both in space and time due to the strong heterogeneity of land surface characteristics, and the short timescales of weather. As a consequence, accurate characterization of LST requires dense spatial and temporal sampling [Li et al., 2013].

Growing recognition of the importance of accurate LST observations has driven rapid advances in remote sensing [Li et al., 2013]. Satellite-based thermal infrared (TIR) data provides LST measurements with high spatial and temporal

*Corresponding author

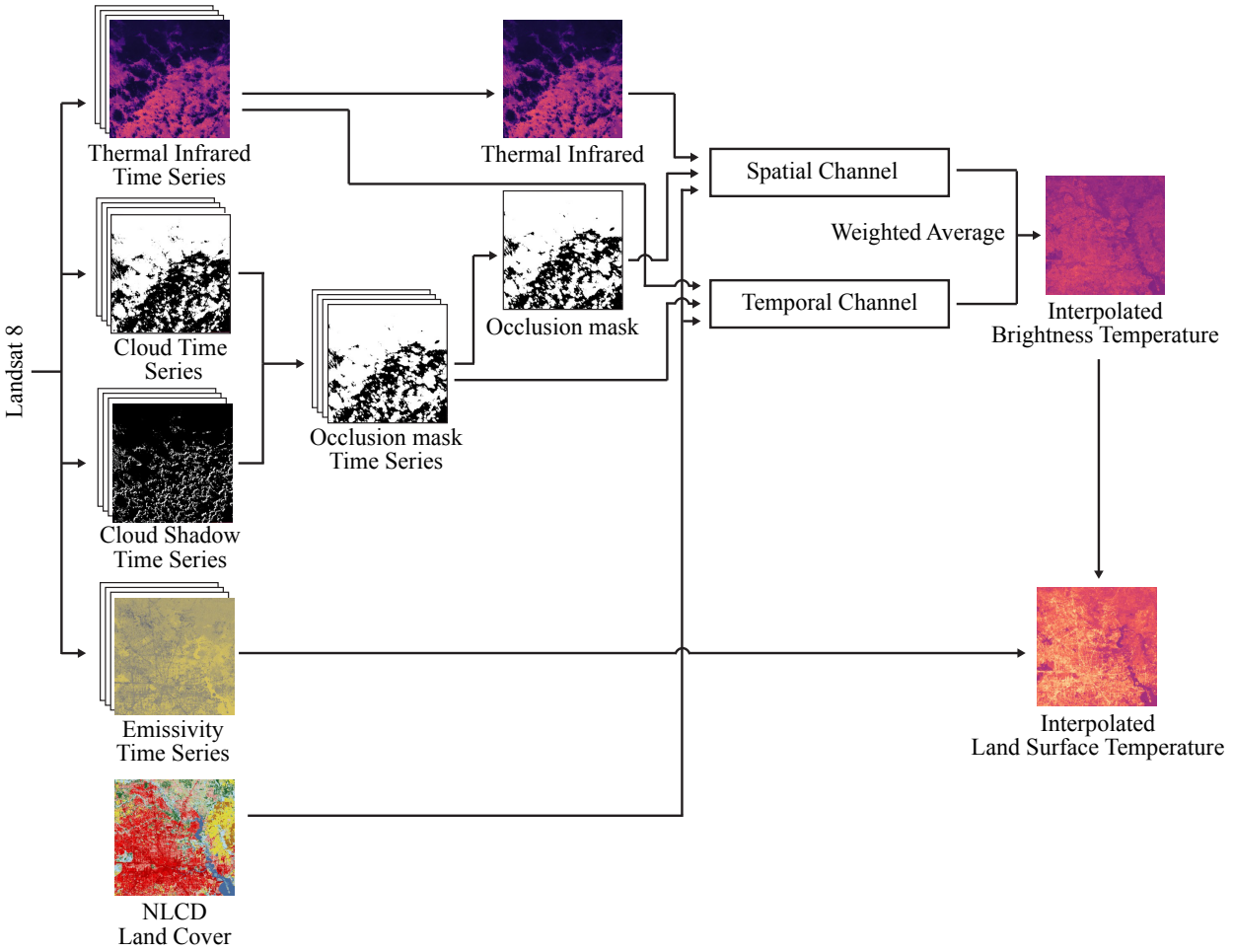

Figure 1: **Schematic overview.** A block diagram of the overall pipeline of our proposed method, ISLAND. We first extract inputs from Landsat 8 and NLCD land cover labels via GEE (leftmost column), and then build an occlusion mask based on cloud and cloud shadow bitmask. ISLAND performs class-aware interpolation using two primary channels: spatial channel and temporal channel. The interpolated BT output is a weighted average between the two channels. Finally, we incorporate emissivity to produce interpolated LST.

resolution at a global scale. As an example, the National Aeronautics and Space Administration (NASA) Landsat 8 satellite was launched in 2013, and its platform has provided detailed TIR data over the last decade [USGS, 2023a,b]. The Landsat 8 and 9 satellites each include a Thermal Infrared Sensor (TIRS) onboard, which collects TIR data at a spatial resolution of 30 m with a revisit cycle of 16 days. The high spatial resolution of TIRS has enabled numerous studies of LST over heterogeneous regions like urban centers [Sobrino et al., 2013, Huang and Wang, 2019, Streutker, 2003] and wetlands [Eisavi et al., 2016, Demarquet et al., 2023].

Despite these advancements, cloud occlusion persists as a substantial obstacle to achieving reliable spaceborne retrievals of LST. Clouds adversely affect TIR readings by blocking thermal radiation emitted from Earth's surface. This results in cloud-contaminated pixels exhibiting considerably lower TIR values compared to their true values, rendering the affected images unusable [Jin et al., 2019]. Additionally, clouds cast shadows on the Earth's surface, which also results in reduced TIR measurements. Depending on the satellite viewing angle and solar angle, cloud shadows further increase the number of contaminated pixels. Unfortunately, cloud contamination is a frequent phenomenon in Landsat images, with studies indicating that an average of 35% of Landsat images globally contain missing data due to cloud contamination [Roy et al., 2008]. Moreover, most cities experience enhanced daytime cloud cover compared to their surrounding rural regions [Vo et al., 2023], making cloud-free TIR images even harder to obtain for cities. Furthermore, regions at higher latitudes, such as Pacific Northwest cities like Portland and Seattle, are prone to cloudier and rainier weather conditions, leading to more frequent cloud contaminations [NOAA, 2020]. Under these circumstances, obtaining a single cloud-free image may be unfeasible for weeks or even months, severely limiting the utility of Landsat TIR data. Collectively, these

barriers have limited practical high spatial and temporal sampling of LST. Thus, the temporal dynamics of LST over complex, heterogeneous terrains remain under-observed, under-studied, and under-constrained, especially at scale.

In this paper, we present a novel method to mitigate the effects of cloud contamination in satellite TIR images. Our method incorporates Tobler's First Law of Geography (TFL), which states that "everything is related to everything else, but near things are more related than distant things" [Tobler, 1970]. In addition to the distance-decay effect from TFL, we also incorporate multi-temporal information and crucially integrate land cover data into our model. Land cover data contains information about physical land types, such as forests, open water, and urban/developed areas. While existing studies have demonstrated the strong relationship between land cover types and LST [Chaudhuri and Mishra, 2016, Zhao et al., 2020, Imran et al., 2021], our model represents the first attempt to utilize land cover to infer occluded TIR pixel values in satellite images. We call our model ISLAND, an acronym for Informing Brightness and Surface Temperature Through a Land Cover-based Interpolator. ISLAND performs interpolation using a set of spatio-temporal filters to capture surrounding pixel values and historical patterns. Notably, these filters are designed to be sensitive to land cover classes, enabling class-specific pattern capture and higher reconstruction accuracy.

We demonstrate that ISLAND provides robust LST reconstruction performance across various occlusion and land cover conditions. Our results indicate that ISLAND greatly improves the practical temporal resolution of Landsat TIR measurements by robustly estimating cloud-contaminated TIR pixels with an accuracy of 1 K. We show three illustrative examples underscoring the utility of ISLAND, namely, (1) urban heat island effects (2) derivation of surface temperature trends, and (3) social vulnerability and urban heat stress.

ISLAND leverages publicly available data from Landsat 8 [USGS, 2023a] and NLCD 2019 [Yang et al., 2018] through Google Earth Engine [Gorelick et al., 2017]. This approach ensures the accessibility and transferability of ISLAND, as it is open-source and can be easily deployed in any region within the continental United States (CONUS) as per user requirements. All source code [2] is available to the public, accompanied by a dataset [3] comprising 20 urban regions with pre-computed ISLAND TIR and LST outputs. We envision that ISLAND will provide tremendous operational value for a variety of applications in Earth, geospatial, and social sciences, and ultimately paves the way for a new generation of LST studies using remote sensing.

2 Related Work

Cloud removal for optical bands: The refinement of cloud-removing algorithms is an open area of research in the field of remote sensing. Many existing studies restrict their analyses to optical bands, measuring surface reflectances in the visible, near-infrared (NIR), and short-wave infrared (SWIR) wavelengths. For example, Zhu et al. [2011] proposed a widely-adopted method named modified neighborhood similar pixel interpolator (MNSPI) that removes thick clouds in Landsat images in Green, Red, and Near Infrared (NIR) bands. MNSPI predicts cloud-occluded reflectance data via an adaptive moving window and a threshold to identify similar pixels using spatial and temporal-based estimations. Cao et al. [2020] proposed an Autoregression to Remove Cloud (ARRC) that uses time series of multi-year land-surface reflectance observations. It reconstructs missing data using the autoregression of Landsat time-series images. The use of multi-temporal references in ARRC leads to higher reconstruction accuracy than MNSPI. Recently, Moreno-Martínez et al. [2020] produces monthly gap-free land surface observations by fusing Landsat observations (30 m, 16-day revisit cycles) with Moderate Resolution Imaging Spectroradiometer (MODIS) observations (500 m, daily revisit cycles) [Wan, 2013]. Broadly speaking, these studies exclude extensions of their methods to TIR channels, and it is unclear how their algorithm would perform given that TIR signals have different dynamics from optical signals. In contrast, ISLAND estimates emitted radiance in the thermal infrared channels rather than estimating reflected radiance in the optical bands. By focusing on TIR signals, ISLAND addresses the unique challenges associated with cloud removal in TIR images, which requires distinct methodologies due to the different nature of TIR radiance.

Cloud removal for LST: Several existing studies develop and discuss cloud removal algorithms for remotely acquired LST. Unfortunately, these algorithms generally target lower spatial resolutions and homogeneous land cover types [Wu et al., 2021]. For example, Yu et al. [2019] proposed a method to reconstruct MODIS LST over cloudy pixels using land energy balance theory and similar pixels, at a spatial resolution of 1 km. Zeng et al. [2015] proposed a spatiotemporal technique to reconstruct MODIS LST products using regression and multispectral ancillary data to classify pixels, which improves reconstruction accuracy. Zhu et al. [2022] reconstruct Landsat 8 LST data using an annual temperature cycle (ATC) model at a spatial resolution of 30 m. Zhu et al. [2022] validated their results against *in situ* LST measurements at six Surface Radiation Budget Network (SURFRAD) sites [Augustine et al., 2000]. Unfortunately, these studies are mainly designed and validated on relatively homogenous regions of land cover, such as cropland, shrubland, and grassland, their results were not demonstrated over urban regions. This study addresses this gap and provides a scalable

[2] https://github.com/Way-Yuhao/ISLAND
[3] https://doi.org/10.17603/ds2-3rf5-sd58

method to generate high-resolution LST, even for highly urbanized regions with complex temperature feedbacks and heterogeneous urban land surface types. We achieve this by explicitly employing NLCD land cover labels and using the satellite LST product with the highest resolution (Landsat 8) to maximize its usability in cities.

Our model shares some of the high-level design principles with existing models, such as the use of historical remote sensing data. To the best of our knowledge, ISLAND is the first algorithm that incorporates land cover labels as ancillary data for cloud removal in LST images. We summarize our *key contributions* as follows: (1) We use NLCD land cover class to accurately reconstruct LST from Landsat 8 TIR inputs. (2) We effectively remove cloud contaminations from Landsat 8 TIR images even under severe occlusion, thereby dramatically improving the temporal resolution of Landsat 8 LST products. (3) Using spatial adjacency and multi-temporal filters, the error in our reconstructed Landsat 8 brightness temperature images is around 1 K. (4) We release a public dataset of cloud-free, reconstructed LST maps for 20 US cities from 2017 to 2022.

3 Methods

Figure 1 shows a schematic detailing the implementation of the model with pseudocode and diagrams. Each stage of the workflow is described in detail in the subsections that follow.

3.1 Data Compilation

We retrieve input data from two major sources. TIR data was first obtained from Landsat 8 TIRS-1 ($10.600 \sim 11.190\,\mu m$), at 30 m resolution [4] and 16-day revisit cycles [Ihlen, 2019]. TIR raw digital numbers (DN) are radiometrically calibrated and converted to at-sensor spectral radiance ($W/m^2 sr \mu m$) and then to at-sensor brightness temperature (BT) (K) following Chander et al. [2009]. We use $T^{TOA} \in \mathbb{R}^{H \times W}$ to denote the at-sensor (or top-of-atmosphere) BT image, where H, W is the height and width of the image, respectively.

Landsat 8 also provides ancillary data relevant to our model, namely, quality assessment bitmask, and emissivity map. The quality assessment system performs cloud cover assessment and generates a bitmask to indicate per-pixel image quality. We refer to this quality assessment bitmask as $Q \in \mathbb{Z}^{H \times W}$, which we later use to derive the cloud and cloud shadow bitmasks. Emissivity $\epsilon \in [0, 1]$ is a measure of an object's ability to emit infrared energy. We use $E \in \mathbb{R}^{H \times W}$ to denote the emissivity map associated with each T^{TOA} image.

For land cover data, we use the National Land Cover Database (NLCD) [Yang et al., 2018] from the U.S. Geological Survey (USGS). NLCD provides spatially referenced descriptive data on the characteristics of the land surface using a set of thematic classes (e.g. urban, forest, and agriculture). NLCD is available for the CONUS region at 30 m resolution with a refresh cycle of once per 3 years. We use the 2019 NLCD release [Dewitz, 2021] and denote it as $L \in \mathbb{Z}^{H \times W}$.

Fig. 1 shows a visual overview of the required inputs listed above. We download all relevant input data via Google Earth Engine (GEE) [Gorelick et al., 2017] and its corresponding Python interface geemap [Wu, 2020]. All layers are spatially aligned with a resolution of 30 m.

Next, we construct an occlusion mask $O \in \{0, 1\}^{H \times W}$ based on the presence of cloud and cloud shadow. At each pixel location $\boldsymbol{p}$, we assign $O_{\boldsymbol{p}} = 1$ if there is either cloud or cloud shadow at this location, and assign $O_{\boldsymbol{p}} = 0$ otherwise. The cloud bitmask is extracted from the 3rd bit of Q, and the cloud shadow bitmask is extracted from the 4th bit of Q.

Using occlusion mask O, we calculate occlusion factor $\theta \in [0, 1]$ that measures the fraction of pixels occluded. Formally, we have $\theta = \frac{\sum_p O_p}{H \cdot W}$. θ is an important metric that measures the severity of cloud contamination. A higher θ indicates more severe occlusion. Finally, we filter out the cloud-contaminated pixels from the BT image. The filtered BT image $\tilde{T}$ is given by:

$$\tilde{T}_{\boldsymbol{p}} = \begin{cases} T_{\boldsymbol{p}}^{TOA} & \text{if } O_{\boldsymbol{p}} = 0 \\ 0 & \text{otherwise} \end{cases} \tag{1}$$

All cloud-contaminated pixels in $\tilde{T}$ have a pixel value of 0. We use this cloud-cleansed BT image $\tilde{T}$ as the input to our interpolation algorithm.

[4] The spatial resolution of Landsat 8 TIR-1 is originally at 100 m and then resampled to 30 m by USGS.

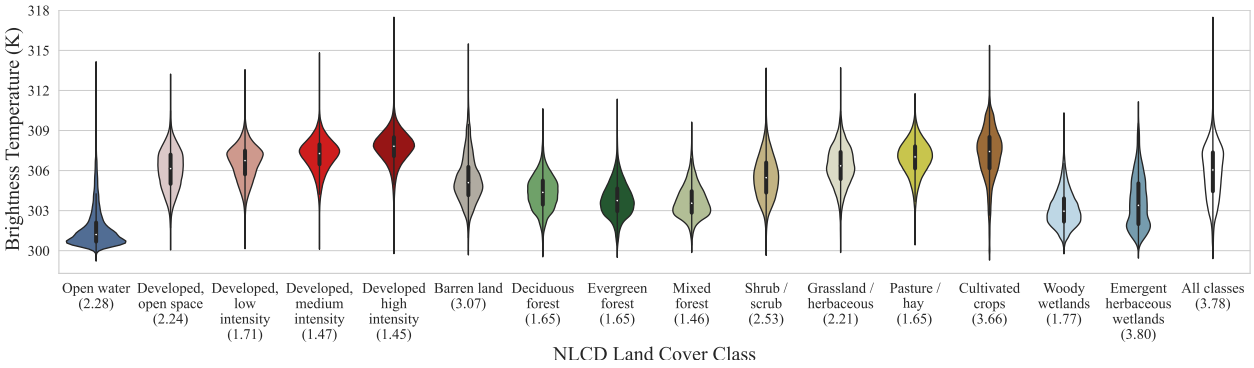

Figure 2: **Motivation: spatial channel.** The violin diagram shows the distribution of BT of San Antonio on August 16th, 2019. The distribution of BT is dependent on land cover, and the variances (in parenthesis) conditioned on individual classes are typically lower than the variance of the parent distribution. When explicitly filtering by land cover class and also by proximity, our spatial channel leads to accurate predictions of BT.

3.2 Interpolator

After acquiring the required inputs from Sec. 3.1, we perform interpolation to predict cloud-occluded pixels. Our interpolator uses two complementary mechanisms: a spatial channel and a temporal channel.

3.2.1 Spatial Channel

In our approach, the prediction of occluded pixel values is informed by leveraging the information embedded in their surroundings. We term this approach the *spatial channel*. The intuition behind the spatial channel is that nearby objects that are in the same land cover class are likely to exhibit similar thermal properties. This approach filters the data based on land cover class, since the distribution of BT is dependent on land cover, as depicted in Fig. 2. The computation of the spatial channel bears a close resemblance to bilateral filtering [Paris et al., 2009]. While traditional bilateral filtering considers variations in pixel intensities of the input image with the aim of preserving sharp edges, the spatial channel uses a different approach, where we filter the input image using the pixel attributes informed by auxiliary images (land cover class L and occlusion O).

Consider our goal to be predicting $\tilde{T}$ at an occluded pixel location $\boldsymbol{p}$. Under a low occlusion factor θ, we estimate $\tilde{T}_{\boldsymbol{p}}$ using a weighted average estimate from other pixels. Conceptually, the weights are determined based on three factors: proximity, land cover class label, and cloud occlusions.

We use a 2D Gaussian filter to model the distance-decay effect. Consider a pixel $\boldsymbol{q}$ within a $f \times f$ neighborhood N centered at $\boldsymbol{p}$. Let $x = \|\boldsymbol{p} - \boldsymbol{q}\|$ be the Euclidean distance between $\boldsymbol{p}$ and $\boldsymbol{q}$. We compute the proximity weight $G_\sigma(x)$ using a Gaussian kernel with standard deviation $\sigma = f/2$:

$$G_\sigma(x) = \frac{1}{2\pi\sigma^2} \exp\left(-\frac{x^2}{2\sigma^2} \right) \tag{2}$$

$G_\sigma(x)$ decreases the influence of distance pixels while prioritizing the influence of nearby pixels.

We further modify the Gaussian filtering so that we only consider $\boldsymbol{q}$ that is cloud-free and has the same land cover class as $\boldsymbol{p}$. Let $\bar{O}$ be the inverse of the occlusion mask O, so that $\bar{O}_{\boldsymbol{q}} = 1$ if there is neither cloud nor cloud shadow at $\boldsymbol{q}$, and $\bar{O}_{\boldsymbol{q}} = 0$ otherwise. To constrain land cover class, let function f_L evaluate the land cover class of two pixels $\boldsymbol{p}$ and $\boldsymbol{q}$ such that $f_L(\boldsymbol{p}, \boldsymbol{q}) = 1$ if the corresponding land cover classes of $\boldsymbol{p}$ and $\boldsymbol{q}$ are the same (i.e., $L_{\boldsymbol{p}} = L_{\boldsymbol{q}}$), and $f_L(\boldsymbol{p}, \boldsymbol{q}) = 0$ otherwise. Formally, we write our weighted average local filter as follows:

$$\tilde{T}_{\boldsymbol{p}} = \frac{1}{\alpha} \sum_{\boldsymbol{q} \in N} G_\sigma(\|\boldsymbol{p} - \boldsymbol{q}\|)\, \bar{O}_{\boldsymbol{q}}\, f_L(\boldsymbol{p}, \boldsymbol{q})\, \tilde{T}_{\boldsymbol{q}} \tag{3}$$

where α is a normalization parameter that ensures weights $\forall \boldsymbol{q} \in N$ sums to 1:

$$\alpha = \sum_{\boldsymbol{q} \in N} G_\sigma(\|\boldsymbol{p} - \boldsymbol{q}\|)\, \bar{O}_{\boldsymbol{q}}\, f_L(\boldsymbol{p}, \boldsymbol{q}) \tag{4}$$

Local filtering (defined in Eq. (3)) works well when the occlusion factor is low. For a high θ, there are fewer neighboring pixels available, and local filtering leads to noisy or even invalid estimations. Instead of local filtering, we resort to global averaging when encountering high θ. Here we estimate the pixel value of $\boldsymbol{p}$ with the average temperature of all non-occluded pixels that have the same land cover class, that is

$$\mu_c = \frac{1}{T} \sum_{\boldsymbol{q} \in \tilde{T} \setminus \{\boldsymbol{p}\}} \bar{O}_{\boldsymbol{q}} \, f_L(\boldsymbol{p}, \boldsymbol{q}) \, \tilde{T}_{\boldsymbol{q}} \tag{5}$$

where c is the land cover class of the occluded pixel $\boldsymbol{p}$, and T is the total number of non-occluded pixels with the same land cover class as $\boldsymbol{p}$, excluding $\boldsymbol{p}$ itself. Contrary to local filtering (Eq. (3)), here the averaging is performed across the entire image, rather than across some local $f \times f$ window. As a result, we are no longer able to capture proximity effects. Therefore, outputs tend to be blurry due to spatial averaging.

Algorithm 1 shows the implementation of the spatial channel. Let $\tilde{T}$ be the occluded BT image as input, f be the size of the local window, and θ^* be the maximum occlusion factor threshold for local filtering. We obtain interpolated image $\hat{T}_{sp}$ as follows:

Algorithm 1 Computation of the spatial channel

Require: $\tilde{T}, f, \theta^*$
if $\theta < \theta^*$ **then** ▷ local filtering
  for $\tilde{T}_p \in \tilde{T}$ **do**
    if $O_p = 1$ **then**
      $\hat{T}_p \leftarrow \frac{1}{\alpha} \sum_{\boldsymbol{q} \in N} G_\sigma(\|\boldsymbol{p} - \boldsymbol{q}\|) \, \bar{O}_{\boldsymbol{q}} \, f_L(\boldsymbol{p}, \boldsymbol{q}) \, \tilde{T}_{\boldsymbol{q}}$
    end if
  end for
else ▷ global averaging
  for $\tilde{T}_p \in \tilde{T}$ **do**
    if $O_p = 1$ **then**
      $c \leftarrow L_p$
      $\hat{T}_p \leftarrow \mu_c$
    end if
  end for
end if
return $\hat{T}^{sp} \leftarrow \hat{T}$

In our implementation, we set the values of the optimization parameters as $f = 75$ and $\theta^* = 0.5$. These values were selected based on extensive testing on a subset of images in our dataset to achieve the best performance.

3.2.2 Temporal Channel

In this section, we show how to generate an interpolated prediction using temporal information. We call this method the *temporal channel*, which is complementary to the spatial channel defined in Sec. 3.2.1. As seen in Fig. 3, the intuition behind the temporal channel is that objects in the same land cover class tend to exhibit similar thermal dynamics over time.

The temporal channel involves four steps: (a) select a set of frames as a reference, (b) preprocess each reference frame via the spatial channel, (c) apply linear adjustments to each reference image, and (d) interpolate occluded regions based on the set of adjusted reference frames.

Reference frame selection: We select reference frames based on two conditions: (i) seasonality and (ii) cloud occlusion. The goal is to identify suitable reference images that can be used to accurately reconstruct occluded BT.

For seasonality, we take into account the temporal offset between the occluded target image $\tilde{T}$ and other available images $\tilde{T}'$. Due to temporal continuity, the previous and the next BT sample over the same region are good reference points. Constrained by the revisit cycle of Landsat 8, the previous and next samples are taken 16 days before and after the target date. In addition to the immediate temporal neighbors, we also leverage the predictable seasonal variations in BT signals. This allows us to include the previous and the next sample acquired in other years as potential references. In

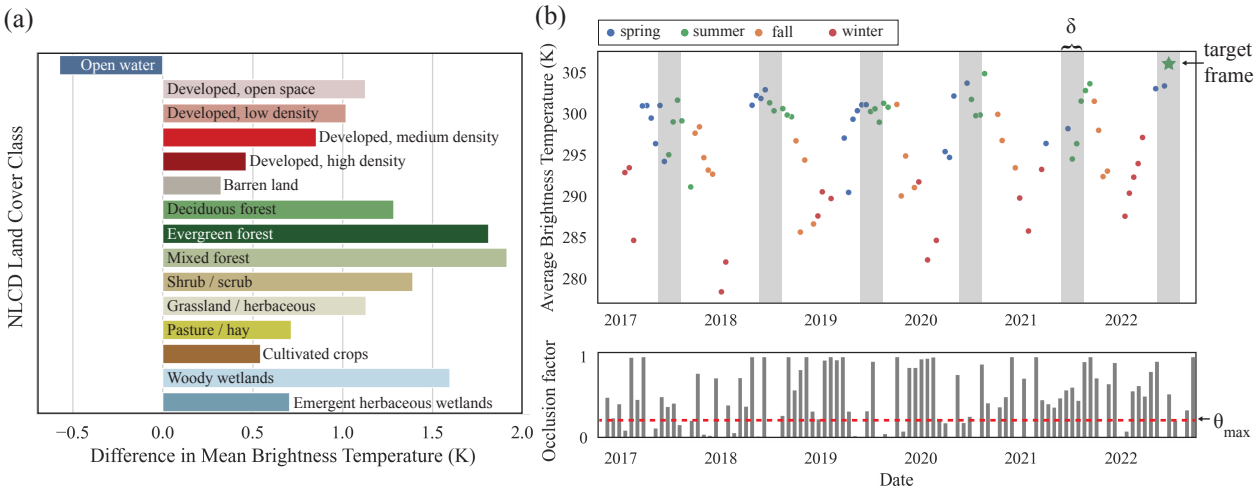

Figure 3: **Motivation for the temporal channel.** (a) The difference in mean BT between Dec 5th and 21st 2018 for each land cover class in Houston. The mean BT for different classes drift in different magnitudes and sometimes at different directions (e.g., water body). This suggests that our temporal-based predictions need to incorporate some mean adjustments tailored to each class. (b) We select reference frames that satisfy two conditions, (i) in the same temporal cycle as the target frame, indicated by gray stripes, and (ii) under a maximum tolerable occlusion factor, θ_{max}. δ denotes the temporal bracket duration.

our actual implementation, we increase the selection limit to samples collected 2 cycles prior to or after the target date in each year, defining the *temporal bracket duration* δ as 2. See vertical gray stripes in Fig. 3(b) for a visual illustration.

The second condition of reference frame selection is the occlusion factor θ. We have observed that minimally occluded reference frames lead to smaller interpolation errors. Therefore we only consider selecting reference frames whose θ is below a certain maximum tolerable threshold, $\theta_{\max}$ (see red dotted line in Fig. 3(b)). We call the set of images satisfying these two conditions candidate reference frames $\mathcal{T}^*_{ref}$. Within $\mathcal{T}^*_{ref}$, we prioritize selecting images that are captured closer to the target frame in time, as measured by the temporal difference $\Delta(|\tilde{T}' - \tilde{T}|)$. To achieve this, we choose a subset of n frames from $\mathcal{T}^*_{ref}$ with the lowest $\Delta(|\tilde{T}' - \tilde{T}|)$. We call this selected subset of reference frames $\mathcal{T}_{ref}$.

Spatial channel pre-processing: Given a selection of reference frames $\mathcal{T}_{ref}$, we apply the computation of spatial channel from Sec. 3.2.1 to produce a set of spatially-complete reference frames. As a result, each pixel contains either observed or interpolated temperature data. Note that the imposed constraint on θ_{max} means that the spatial channel only needs to interpolate a minimal amount of occlusion.

Linear adjustments: After pre-processing $\mathcal{T}_{ref}$, we apply a linear adjustment to all pixels in each class. Fig. 3(a) shows that the changes in mean BT (denoted as μ_c) can differ drastically between classes. Although the selection of reference frames helps mitigate these discrepancies, some adjustments are still necessary. Specifically, for each reference frame, we add the difference in μ_c (i.e., $\Delta\mu_c$) between two dates to all pixels belonging to the corresponding land cover class. $\Delta\mu_c$ visually translates to the length of each bar in Fig. 3(a). We repeat this process for all images in $\mathcal{T}_{ref}$.

Reference frame-based interpolation: After the previous two steps, we obtain a set of linearly-adjusted reference frames. The interpolated BT image, $\hat{T}^{temp}$, is the average of each linearly adjusted reference frame. This interpolation step combines the information from multiple reference frames to produce a spatially complete and temporally consistent estimate of the occluded BT image.

Algorithm 2 shows the implementation of the procedures above. Let n be the number of reference frames to be selected, δ be the temporal bracket duration, and θ_{max} be the maximum tolerable occlusion factor. We compute the interpolated image $\hat{T}_{temp}$ as follows:

Algorithm 2 Computation of the temporal channel

Require: $\tilde{T}, n, \delta, \theta_{max}$
1: $\mathcal{T}^*_{ref} = \{\tilde{T}' \in \mathcal{T} | \delta_{\tilde{T}'} < \delta \wedge \theta_{\tilde{T}'} < \theta_{max}\}$ ▷ Reference set conditions
2: $\mathcal{T}_{ref} = \min_{\Delta(|\tilde{T}'-\tilde{T}|)} (T' \in \mathcal{T}^*_{ref})_{(n)}$ ▷ Reference frame selection
3: **for** $\tilde{T}' \in \mathcal{T}_{ref}$ **do**
4: $\quad \hat{T}' \leftarrow \mathrm{SP}(\tilde{T}', f, \theta_{min})$ ▷ Preprocess via spatial channel
5: $\quad \Delta\mu_c = \frac{\sum_{p \in P_c} |\tilde{T}_p - \tilde{T}'_p|}{|P_c|} \; \forall c$
6: $\quad \tilde{T}'_p \leftarrow \tilde{T}'_p + \Delta\mu_c \; \forall p \in T_c \; \forall c$ ▷ Linear adjustments
7: **end for**
8: **return** $\hat{T}^{temp} \leftarrow \mathrm{average}(\mathcal{T}_{ref})$ ▷ Interpolate

We set $n = 3$, $\delta = 2$, and $\theta_{\max} = 0.1$. SP$(\cdot)$ denotes the function for spatial channel defined in Algorithm 1, and f and $\theta_{\min}$ at line 4 follow their default values from Sec. 3.2.1. The subscript $\cdot_{(n)}$ used in line 2 signifies the first n elements of the sequence, arranged according to the minimization criterion. P_c is the set of all pixel locations where the corresponding land cover class is c, and $|P_c|$ is the cardinality of set P_c.

3.2.3 Brightness Temperature Interpolation

Following the previous two subsections, we acquire initial predictions $\hat{T}^{sp}$ from the spatial channel and $\hat{T}^{temp}$ from the temporal channel. The final interpolated brightness temperature, denoted as $\hat{T}^{BT}$, is calculated as the weighted average of the two initial predictions:

$$\hat{T}^{BT} = w \cdot \hat{T}^{sp} + (1 - w) \cdot \hat{T}^{temp} \tag{6}$$

where we set the weight $w = 1 - \theta$. Note that for a minimally occluded image (a small θ), more weight is assigned to the spatial channel. Contrarily, for a severely occluded image (a large θ), fewer neighboring pixels are available for the spatial channel, and more weight is assigned to the temporal channel accordingly.

3.3 Emissivity Compensation

The interpolated BT image $\hat{T}^{BT}$ differs from LST by assuming all ground objects are ideal black body radiators (i.e., $\epsilon = 1$, where ϵ is emissivity). We derive the estimated LST, denoted as $\hat{T}^{LST}$, as follows:

$$\hat{T}^{LST} = \frac{1}{E} \circ \hat{T}^{BT} \tag{7}$$

where E is the emissivity map for Landsat 8 TIRS-1 estimated by ASTER GED [Hulley et al., 2015], and $\circ$ is element-wise multiplication. Similar to thermal infrared channels, cloud contamination also affects ASTER GED estimation [Cook et al., 2014], albeit only to a certain extent. Here we accept ASTER GED estimations without further consideration of its susceptibility to cloud contamination. For a more comprehensive discussion on the limitations of this step, please refer to Section 5.1. This completes the process of deriving the interpolated BT ($\hat{T}^{BT}$) and LST ($\hat{T}^{LST}$) values.

4 Results

4.1 Public Data Products

We deploy ISLAND across 20 regions in the United States. These regions are selected for having the highest populations, as reported in the 2020 U.S. Census [United States Census Bureau, 2023]. For each region, we manually define a polygon roughly covering the metro region for each city [5]. We collect satellite data from January 1st, 2017 to July 1st, 2022 using the data compilation process described in Section 3.1. We then process each region using ISLAND following Sec. 3.3. ISLAND produces geo-referenced GeoTiff files for both BT and LST at a spatial resolution of 30 m every 16 days [6] for each observation region. Our public dataset is available on the NHERI DesignSafe Cyberinfrastructure [Rathje et al., 2017] at the following DOI: https://doi.org/10.17603/ds2-3rf5-sd58 [Liu et al., 2023].

[5] Due to the 32 MB limit per image download from Earth Engine, the polygon may not encompass the entire metro region for some cities, such as New York City.

[6] Subject to data availability and requires $\theta < 0.99$

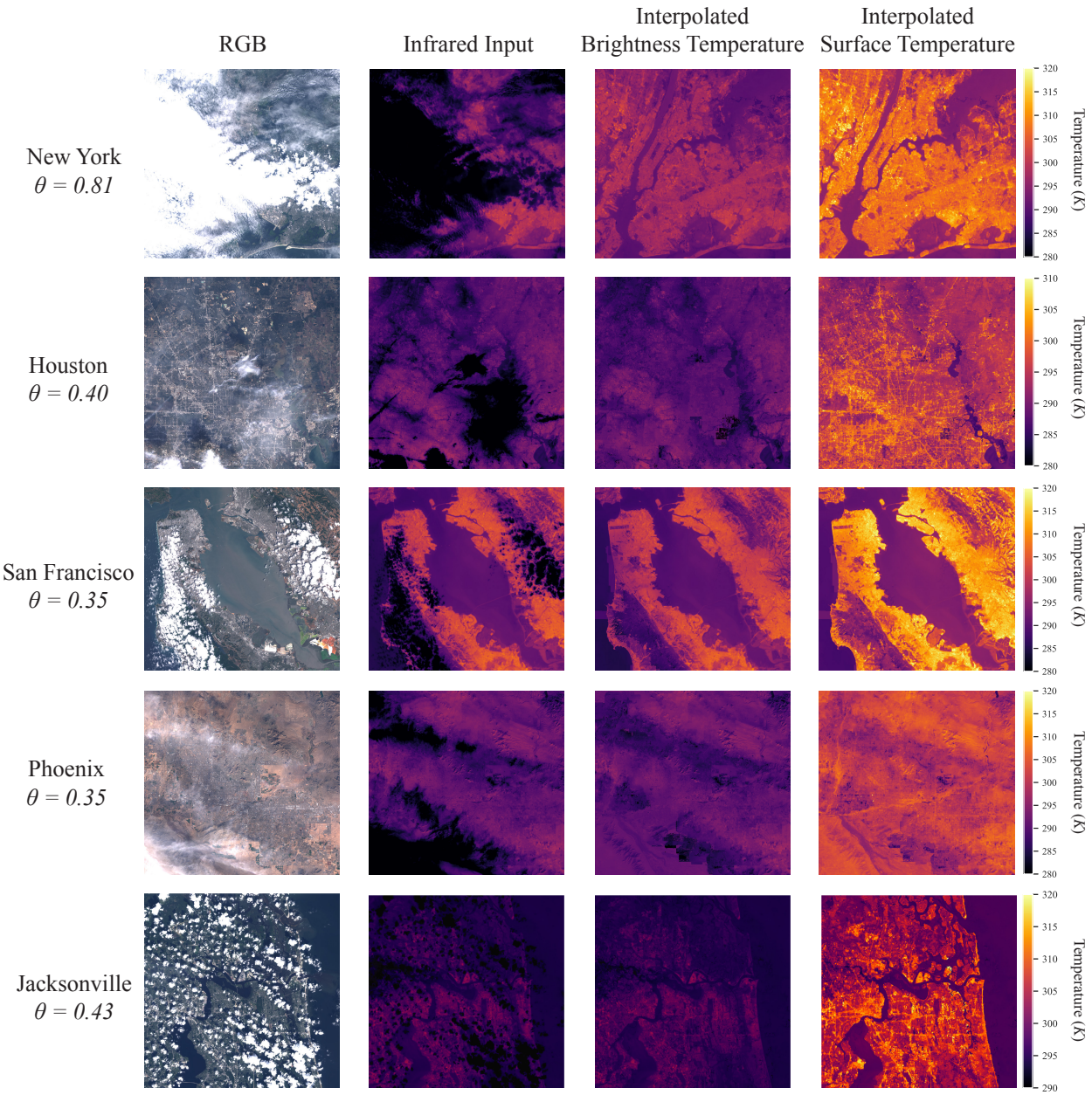

Figure 4: **Results.** ISLAND performs robust interpolation under a variety of surface land cover and cloud occlusion conditions. We show our interpolated BT and LST outputs alongside TIR inputs, and RGB images for visual reference. The fraction of pixels occluded is denoted as θ.

Table 1: **Evaluation metrics for validation and ablation study.** We introduce synthetic occlusion by randomly overlaying tiles onto the input TIR images, thereby zeroing TIR pixel values. We show MAE and RMSE for these synthetically occluded areas for different cities. We also vary the size of occlusion *s*, and the maximum number of occlusion tiles *n*. ISLAND (marked as M1) is compared against other models in an ablation study. Legends: **M1**: ISLAND; **M2**: spatial channel only; **M3**: temporal channel only; **M4**: No NLCD input; **M5**: Naive average.

Parameters			MAE (K) ↓					RMSE (K) ↓				
City	*s*	*n*	**M1**	M2	M3	M4	M5	**M1**	M2	M3	M4	M5
Houston	250	10	**1.07**	1.20	1.07	1.37	2.27	1.38	1.56	**1.37**	1.71	2.68
Houston	750	3	1.12	1.34	**1.00**	1.51	2.22	1.43	1.71	**1.30**	1.86	2.65
Phoenix	500	1	1.58	1.67	**1.10**	1.67	2.04	2.09	2.22	**1.43**	2.19	2.57
Denver	50	1	**1.43**	1.58	1.62	1.58	2.22	**1.75**	1.93	1.90	1.91	2.58
New York	100	2	0.96	1.02	**0.91**	1.53	2.72	1.38	1.36	**1.32**	1.91	3.12
Jacksonville	75	2	**0.82**	0.86	0.96	1.19	2.06	**1.06**	1.14	1.19	1.47	2.41

Fig. 4 shows a set of interpolated LST maps. We choose a diverse set of examples consisting of different land cover and cloud occlusion conditions. ISLAND reconstructs spatially complete BT and LST maps under a variety of conditions, from lightly occluded by thin cirrus clouds (Phoenix) to heavily occluded by optically thick clouds (New York, 81% occluded). Our model performs well across regions with different land cover characteristics, from dense urban settings (New York, San Francisco) to diverse wetlands (Jacksonville).

4.2 Error Analysis

In this section, we perform a quantitative analysis of model performance. In the derivation of LST, multiple steps in the data retrieval have been shown to be error-prone, including sensor calibration, atmospheric transmission, and uncertainty in the estimation of emissivity [Li et al., 2013]. We restrict our error analysis to the interpolation of TIR and ignore factors external to this process. In particular, since we employ an existing product ASTER GED [Hulley et al., 2015], which itself introduces error under cloud occlusion [Cook et al., 2014], we conduct error analysis on BT instead of LST.

4.2.1 Validation

We artificially introduce image occlusion to use as validation. We call these occlusions *synthetic occlusions*. To introduce synthetic occlusions over an arbitrary region, we simply overwrite pixel values of the TIR input image to zero and mark the corresponding pixels in the occlusion mask as True. ISLAND discards all thermal data in the occluded region regardless of whether the occlusion is real or artificially induced. We treat the un-occluded, original image, as the true LST, and perform evaluations between the true LST and estimated LST over synthetically-occluded regions. The locations of synthetically-occluded regions are randomly selected for fairness.

We artificially overlay occlusion for 5 different regions. For each region, we randomly generate at most *n* squares of length *s* as synthetic occlusions. We repeat this experiment for all available observation dates for each region, including dates with actual cloud occlusions (i.e., *real* occlusions). For images with real occlusion, we simply place synthetic occlusions alongside real occlusions. We ensure that the overlap is minimal, both between different synthetic occlusion tiles, and between synthetic occlusion and real occlusion. Note that parameter *n* is the maximum number of synthetic occlusion tiles to be applied to images, the actual number of tiles being placed in each image will vary and will be lower for images with more real occlusion.

Table 1 shows the validation results for the 5 selected regions. M1 refers to our model ISLAND, while M2 to M5 refers to other models discussed in Sec. 4.2.2. For each region, we show both the mean absolute error (MAE) and root mean squared error (RMSE) over the synthetically occluded regions.

Effects of regional characteristics on performance: MAEs are in the range of 0.82 K to 1.58 K for the 5 validation regions. The region with the lowest (best) MAE and MSE score is Jacksonville, a region with diverse surface land cover types. This suggests that ISLAND tends to perform with higher skill in regions with a heterogeneous set of land cover labels. By contrast, MAE and MSE are both the highest for Phoenix, a region where thin cirrus clouds are frequently observed. Due to the low opacity of cirrus, we encounter numerous scenarios where cirrus are mislabeled (false negative labels). Since even cirrus with a low optical thickness block thermal transmission to some degree, we observe underestimated BT and LST reconstructions in regions occluded by cirrus. Row 4 in Fig. 4 confirms this

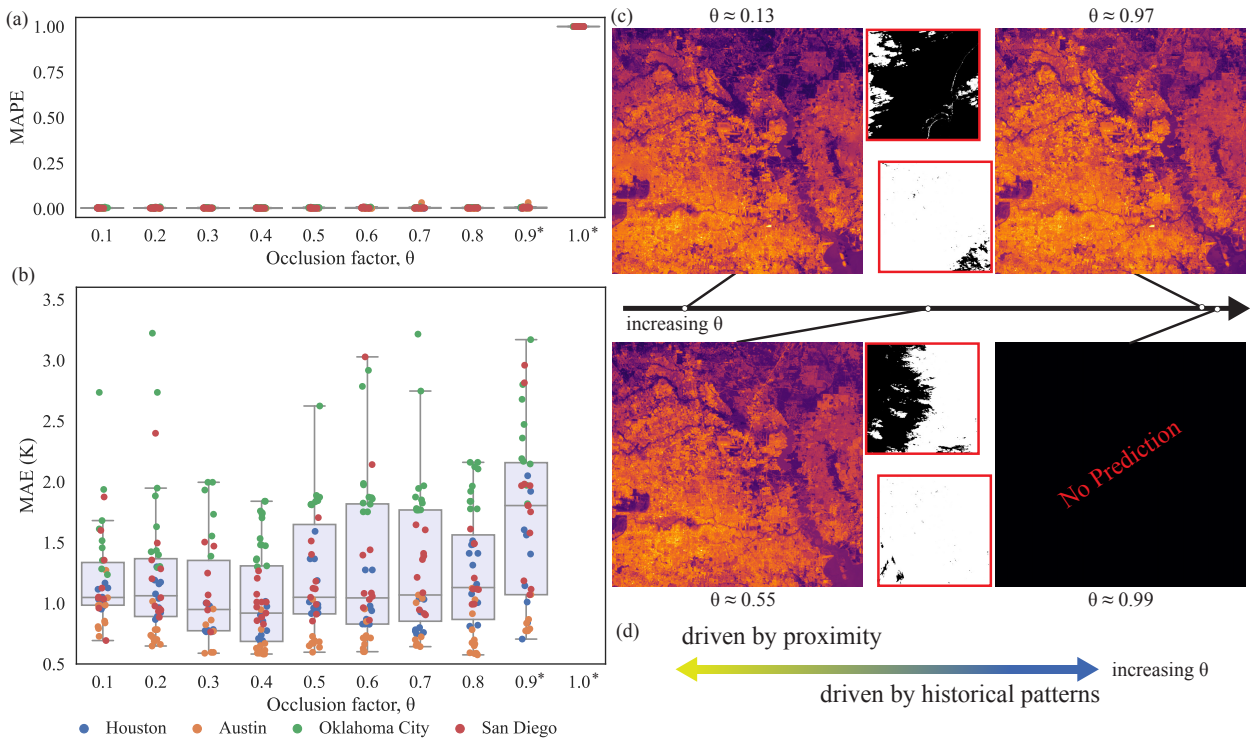

Figure 5: **Performance degradation with increasing occlusion factor.** For each region, we choose one cloud-free scene, and overlay a set of synthetic occlusions. (a) MAPE in synthetically-occluded regions for different ranges of θ. (e.g., the first bar corresponds to samples where $0 \leq \theta < 0.1$. The last two bars denoted by * have special ranges $0.9 \leq \theta < 0.99$ and $\theta \geq 0.99$, respectively) (b) MAE in synthetically occluded regions for different ranges of θ. (c) ISLAND BT outputs at different θ alongside the corresponding synthetic occlusions. (d) Predictions are primarily driven by the proximity effect for small θ, and by historical patterns for large θ.

observation, where some part of the cirrus is, in fact, mislabeled, coinciding with lower estimated BT and LST values under cirrus. We suspect inaccurate cloud labeling contributes to higher errors for Phoenix.

Effects of occlusion characteristics on performance: Table 1 indicates larger errors are generally associated with heavier synthetic occlusions. However, our ability to quantify this effect is limited because the synthetic clouds are rectangular tiles, unlike real clouds. In this subsection, we take a closer look at how ISLAND reacts to different occlusion scenarios. Instead of overlaying rectangular tiles, we sample existing occlusion masks in our dataset shown in Fig. 1. These occlusions include both cloud and cloud shadow, and are much more complex in terms of shape, patterns, etc. We apply data augmentation (random horizontal and vertical flipping) to increase diversity and data sample size, and resize occlusion masks to make their dimensions align with the cloud-free TIR image. Implementing occlusion involves setting the TIR pixel values to zero in the presence of synthetic occlusions and marking the corresponding occlusion mask pixels as True. As seen in Fig 5, we choose 4 regions to investigate, namely, Houston, Austin, Oklahoma City, and San Diego, and overlay 100 different occlusions per city. The cloud-free TIR images were captured on April 14, 2020, August 16, 2019, July 19 2019, and November 12, 2018 for each city, respectively. We plot both MAE and Mean Absolute Percentage Error (MAPE) on reconstructed BT against different ranges θ, [0, 0.1), [0,1, 0.2), ..., [0.8, 0.9). We further divide the last bins (indicated by *) into [0.9, 0.99), and [0.99, 1]. Fig.5(a) shows that MAPE stays below 1% for all $0 \leq \theta < 0.99$, except for two outliers at $\theta = 0.93$ and 0.79 where MAE $\approx$ 3%. Fig.5(b) provides a zoomed-in view on the range $0 \leq \theta < 0.99$. The mean MAE remains close to 1 K for $\theta < 0.9$, before rising to approximately 2 K at $0.9 \leq \theta < 0.99$. Above $\theta \geq 0.99$, there is a jump discontinuity in performance, where MAPE approaches 100%. Interestingly, ISLAND's performance is not uniform across all 4 cities tested here; Austin has the lowest error and

Oklahoma City has the highest error. One hypothesis for such discrepancies in performance across regions is that if high-quality reference frames are readily available (e.g. mid-August for Austin), then ISLAND tends toward better performance by taking advantage of its temporal channel and utilizing accurate multi-temporal data.

To visualize the results, Fig. 5(c) shows ISLAND BT outputs at different values of θ, namely $\theta \approx 0.1$, 0.5, 0.94, and 0.99. There are small visual discrepancies between these outputs. At $\theta \approx 0.13$, the spatial channel produces a slightly blurry and noisy prediction on the left side of the image, where pixels are occluded. At $\theta \approx 0.55$, the right half of the image is slightly blurrier than the left half, likely due to the equal average of the two channels and the lack of diversity of land cover labels in the western area of Houston. At $\theta \approx 0.94$, ISLAND produces surprisingly sharp and accurate results, with the texture of the image being primarily driven by historical patterns and land cover class labels. However, at $\theta \approx 0.99$, ISLAND fails to produce any outputs, resulting in an empty prediction. This trade-off between proximity and historical pattern based on θ is illustrated in Fig. 5(d).

4.2.2 Ablation Study

To further demonstrate the effectiveness of our model, we perform an *ablation study* [7] , where we remove key components of our model and observe the impact of each of these components on the overall performance. Table 1 shows a list of models. M1 refers to our full model ISLAND. In M2, we exclude the temporal channel and only keep the spatial channel. In M3, we discard the spatial channel and only keep the spatial channel. M4 is the same as ISLAND, except we remove NLCD land cover labels as input. M4 adopts a simplified approach where missing values are replaced with the average pixel value within an image, without considering their spatial distribution or land cover class.

It is worth noting that ISLAND (M1) is a composite of outputs generated by M2 and M3, making it reasonable to expect that the performance metrics of M1 would lie between those of M2 and M3. Notably, when confronted with heavier occlusions (indicated by a large θ), M3 consistently emerges as the top-performing model. This finding highlights the effectiveness of relying solely on the temporal channel in such challenging scenarios. Conversely, for occlusions of low to moderate severity, the spatial channel exhibits superior performance over the temporal channel, thus positioning M1 ahead of M3. This observation implies that our devised weighting scheme (Eq. (6)) effectively captures the characteristics of the spatial and temporal channels. By appropriately favoring the temporal prediction in the presence of heavy occlusions and the spatial prediction for lighter occlusions, our weighting scheme strikes a balance that optimizes the overall performance of ISLAND. These findings provide valuable insights into the interplay between the spatial and temporal components of our model and validate the design choices made in ISLAND. The weighted combination of the two channels allows for adaptability to varying occlusion levels, enhancing the model's robustness and accuracy in capturing land surface temperature under diverse conditions.

Both the validation and ablation studies demonstrate that our model is robust in performance and is able to generalize reasonably well to different regions in the U.S. and under different occlusion characteristics.

4.3 Applications

In this section, we show a set of applications demonstrating the impact of ISLAND for a variety of applications of LST in urban environments.

4.3.1 Deriving surface temperature trends

A direct product of our model is the derivation of BT and LST. The robustness demonstrated in Section 4.2 and the compelling results displayed in Figure 4 underscore the model's ability to generate accurate interpolated BT and LST values across a wide range of conditions, with the only constraint being that the occlusion factor $\theta < .99$. As highlighted in Section 1, previous studies investigating changes in land surface temperature through remote sensing have been constrained by limited observational conditions, restricting their analyses to a fraction of dates characterized by minimal cloud occlusion [Sobrino et al., 2013, Huang and Wang, 2019, Gomez-Martinez et al., 2021, Baiocchi et al., 2017]. However, with the introduction of ISLAND, these limitations become obsolete, granting access to a significantly expanded set of operational thermal data, particularly in urbanized regions.

Beyond the production of interpolated image outputs, ISLAND enables the examination of temporal variations in LST on daily-to-seasonal timescales. By reconstructing skillful LST maps for the majority ($\theta < .99$) of observation dates, ISLAND enables the comparison of thermal behaviors for a given region across time, at a relatively dense sampling rate of every 16 days, and encompassing diverse land cover types. To illustrate this capability, Figure 6 showcases

[7] Not to be confused with the glaciological definition of ablation, which refers to the process of removing snow, ice, or water from a glacier or a snow field. Here we use the artificial intelligence definition of ablation study, where certain parts of a network are removed in order to gain a better understanding of the model's behavior.

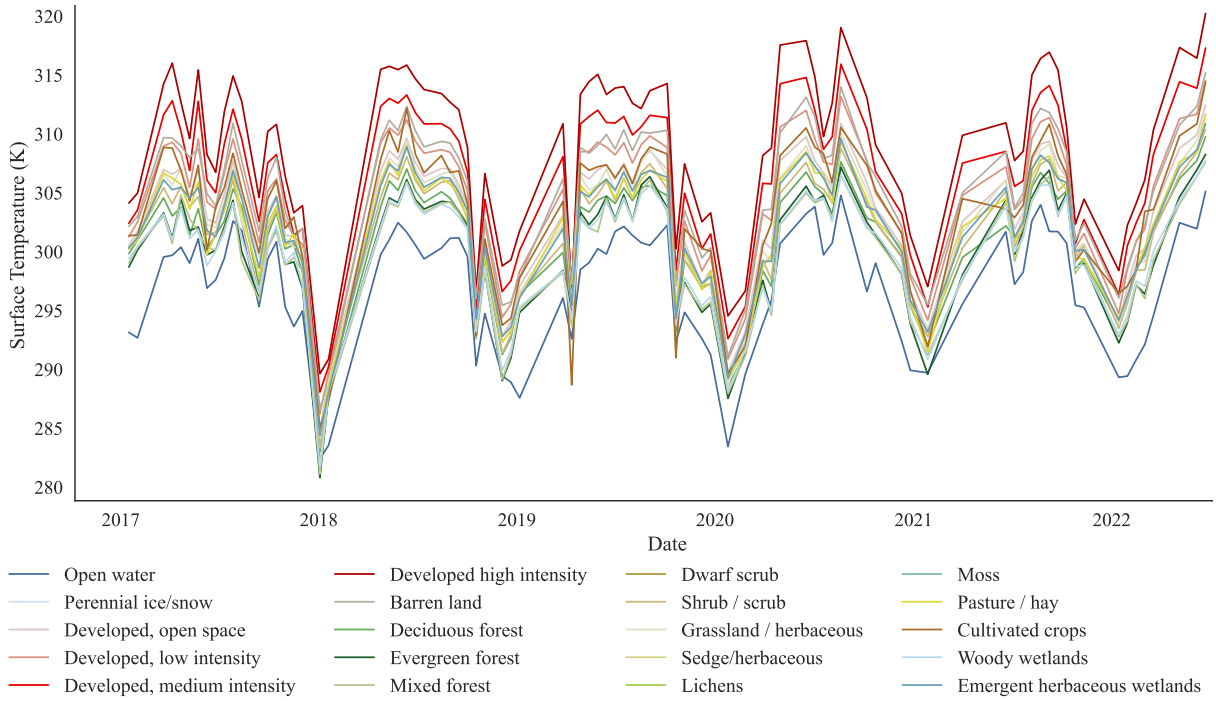

Figure 6: **Changes in mean surface temperature, 2017-2022.** Mean LST for different NLCD land cover classes in Houston over the span of 5.5 years. By providing temporally consistent LST outputs, ISLAND enables time-series analysis of LST.

the evolution of surface temperature in Houston. Each colored line represents the average LST for a particular land cover class for all grid cells over Houston. Pronounced temperature seasonality is evident in the time series from 2017-present, with clear changes in seasonal structure from year to year. The ability to partition surface temperatures retrieved from different land cover types reveals differences of up to 15°C between forested, water-covered surfaces and urban developed surfaces (e.g. open-water vs. developed high intensity). With a 16-day temporal resolution, one can evaluate temperature distributions and variances over different land cover classes in different seasons. ISLAND facilitates an in-depth investigation of the temporal dynamics of surface temperature within any region located in the CONUS, providing valuable insights for climatological and ecological analyses.

4.3.2 Urban heat island effects

Another key application of our model is the ability to study urban heat island effects (UHIE) [Moller et al., 2022] at high spatiotemporal resolution. UHIE refers to the phenomenon that urban areas are significantly warmer than their surrounding rural areas. UHIE is primarily driven by the differences in thermal absorption between different materials. For example, grass- or water-covered surfaces tend to have lower temperatures than concrete and asphalt. By providing high spatial and temporal resolution LST outputs, ISLAND offers a novel data product for identifying, studying, and monitoring UHIE in major U.S. metropolitan areas. Fig. 7 shows maps of three of the largest U.S. metropolitan areas, Los Angeles, Chicago, and Houston, where the pixel values indicate the number of days surpassing a region-specific temperature threshold. The thresholds are selected based on the definition of *Extreme Danger* from the National Weather Service (NWS) heat index [Rothfusz and Headquarters, 1990]. The NWS heat index is a function of both temperature and relative humidity. The Comparative Climatic Data (CCD-2018) [NOAA, 2020] provides the morning annual average relative humidity (R) for each city. We select the LST threshold for each region as the minimum ambient dry bulb temperature that meets the NWS Extreme Danger criteria for the city's corresponding R. The range of observations is 4.5 years, at a sampling rate of once per 16 days. Higher values in the frequency maps indicate a more frequent occurrence of UHIE. These frequency maps are available at 30 m resolution and can be easily computed using our public dataset. From an urban planning perspective, these UHIE frequency maps offer a powerful tool for enhancing our understanding of how land cover choices influence micro-climates, heat extremes, and the associated health risks. By providing insights into the spatial distribution and frequency of UHIE, these maps can inform decision-making

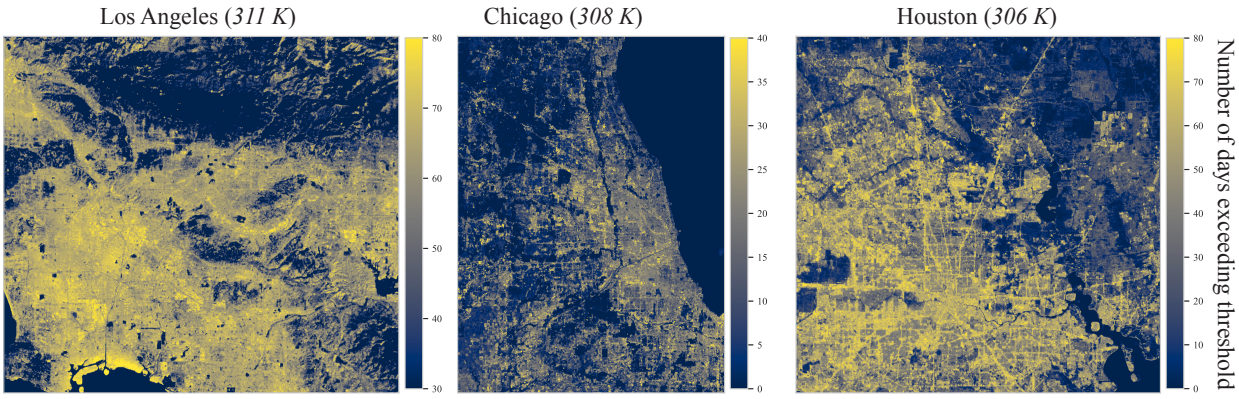

Figure 7: **Urban heat island effects in Los Angeles, Chicago, and Houston.** Each figure panel shows the *number of days* in which the LST at each pixel location exceeds a predetermined threshold (shown in parentheses). The temperature threshold for each city is chosen based on the definition of *Extreme Danger* from the National Weather Service heat index.

processes regarding urban development and land cover management, aiming to mitigate the adverse effects of heat on public health and well-being.

4.3.3 Social Vulnerability & Urban Heat Stress

As illustrated in the last two applications, ISLAND facilitates the development of comprehensive datasets of LST and UHIE. The developed datasets will enable better characterization of heat exposure and its impacts on social, infrastructure, and environmental systems. A representative example application would be to investigate inequities in urban heat exposure. Given the health, well-being, and quality of life implications of urban heat, and initiatives like Justice 40 [The White House, 2022], which call for federal climate investments to be directed to environmental justice communities, understanding the equities in urban heat exposure can centrally guide prospective investments. For example, quantifying inequities in exposure to urban heat will help design adaptation measures such as increasing vegetation cover or guiding urban planning, among others.

The distribution of UHIE for residential areas and the social vulnerability of the exposed population for a few cities are shown in Figure 8. Here, social vulnerability is measured using the Centers for Disease Control and Prevention Social Vulnerability Index (CDC SVI) [Centers for Disease Control et al., 2020]. The CDC SVI measures social vulnerability on a scale of 0 (least vulnerable) to 1 (most vulnerable), taking into account socioeconomic status (e.g., housing cost burden), household characteristics (e.g., civilian with a disability), racial and ethnic minority status (e.g., Hispanic, Alaska Native), housing type and transportation factors (e.g., no vehicle). The latest available residential land use data (2016) from Mc Shane et al. [2022] are used to identify residential regions. Additionally, UHIE is calculated as the number of days that a pixel (resolution of 30 m $\times$ 30 m) exceeds a land surface temperature threshold of 35 °C (308.5 K). Only pixels with at least one day of temperature over the threshold are considered for the analysis.

From Figure 8, many cities show a systemic inequity in heat exposure. For example, in Los Angeles, socially vulnerable communities are exposed to high urban temperatures compared to less socially vulnerable communities (Pearson's correlation, $r = 0.45$). A similar trend can be seen in cities such as San Antonio ($r = 0.36$), San Francisco ($r = 0.44$), San Jose ($r = 0.44$), and New York ($r = 0.34$). In contrast, cities such as Houston ($r = 0.00$), Phoenix ($r = 0.16$), Jacksonville ($r = 0.08$), Fort Worth ($r = 0.02$), and Austin ($r = 0.09$) show no or negligible inequity in urban heat exposure. Factors ranging from vegetative cover to colocation with industrial or commercial locations might influence urban heat exposure. By providing reliable and more complete datasets to quantify UHIE, this study will allow for a better understanding of the factors influencing heat exposure and, as a result, will aid in developing strategies to mitigate urban heat stress.

While this section only provides three case studies, the proposed method facilitates many applications requiring high-resolution site-specific data. Some example applications include designing building envelopes and Heating, Ventilation, and Air Conditioning (HVAC) systems, investigating the influence of thermal stresses on infrastructure aging and deterioration, power system reliability, and energy demand shifts, or even high-resolution weather and natural hazard modeling that accounts for fine-scale surface temperature effects.

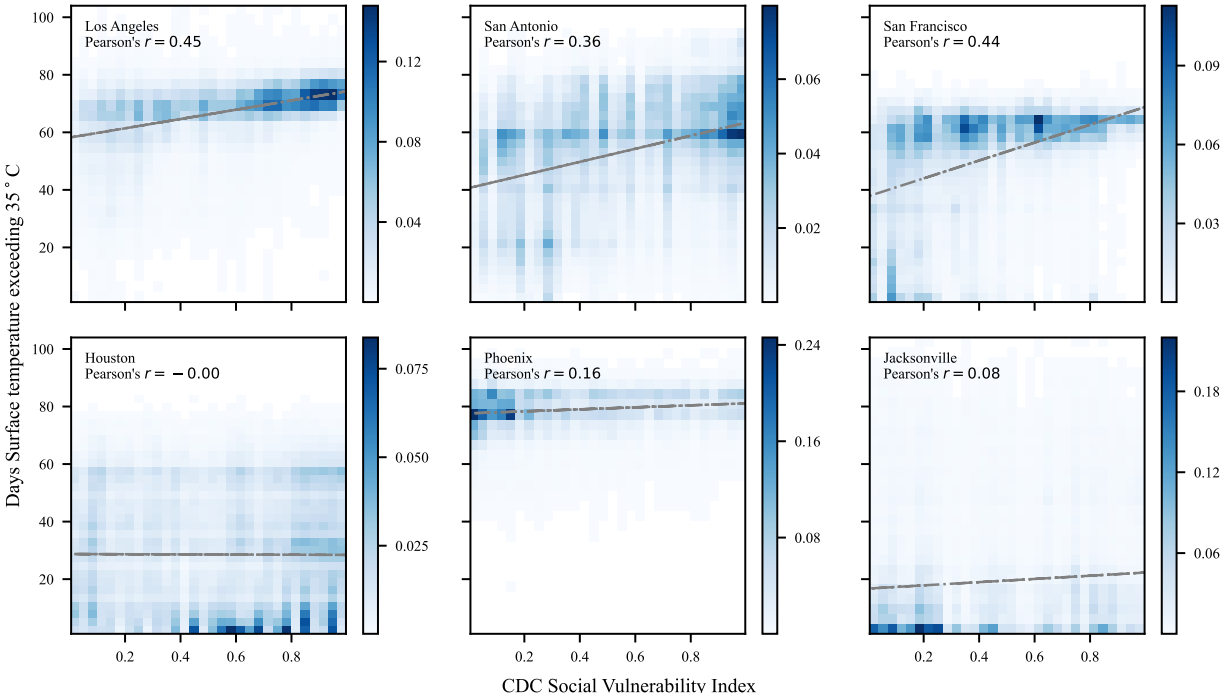

Figure 8: **Equity in exposure to urban heat island effect.** Each figure panel shows a density plot mapping the relationship between the *number of days* in which the LST of a pixel exceeded 35°C and their social vulnerability measured using CDC Social Vulnerability Index. Here we restrict our analysis to residential areas within each city.

5 Discussion & Conclusions

5.1 Assumptions and Limitations

Despite the demonstrated validity and effectiveness of ISLAND, the model does contain important assumptions and limitations.

Design philosophy of cloud removal in thermal images: In this paper, we introduced a method to predict BT and LST in occluded regions. Unlike occlusion removal techniques applied to RGB images, cloud occlusions have distinct characteristics that locally and temporarily influence the thermal behavior of the Earth's surface. Clouds have high albedo, reflecting incoming solar radiation and thereby shading the surface, which leads to a decrease in surface temperature [Jin et al., 2019]. Additionally, depending on cloud altitude and composition, some clouds can absorb outgoing longwave radiation emitted by the Earth's surface and re-emit heat, resulting in surface warming. Furthermore, condensation during cloud formation releases heat locally to the environment [USGS, 2019]. These complex cloud processes collectively contribute to alterations in measured surface temperature, and by removing clouds from the thermal images, we inherently eliminate the ability to account for cloud-surface temperature feedback in our analyses.

We want to reiterate that the primary objective of our work is to estimate a *hypothetical* land surface temperature (LST) of ground objects under cloud-free conditions. We believe that this assumption is reasonable and valid within the context of periodic Earth observations, considering the highly transient nature of clouds [Cotton et al., 2011]. Satellites in the Landsat program operate in sun-synchronous orbits (SSO) [Boldt-Christmas, 2020], meaning that every satellite passes through an arbitrary site at a constant local time while maintaining a fixed solar angle. The temporal consistency of these observations allows researchers to compare changes at Earth's surface over time. Our work serves as a valuable addition to the Landsat program by addressing the challenge of cloud contamination and mitigating its effects. Here we argue that local disruptions in temperature caused by clouds should not be considered, especially for isolated, short-lived, small areas of cloud cover.

Difficulties of *in situ* validation: The quantitative assessment of our model's performance in occluded regions under real-world conditions poses significant challenges. Validating satellite-derived land surface temperature (LST) measurements,

even in cloud-free regions, is a complex task. The complexity arises from the need to obtain accurate *in situ* LST measurements at the scale of satellite measurements, and the inherent spatiotemporal variations in LST [Li et al., 2013].

We acknowledge the limitations and complexities associated with *is situ* LST validation. First, acquiring sufficient and appropriate ground truth LST data is challenging. While it is theoretically possible to gather *in situ* thermometer measurements through weather stations (e.g., National Weather Service), there are fundamental differences between near-surface air temperature measurements obtained by weather stations and LST [Li et al., 2013]. An alternative approach to weather stations is ground-level thermal cameras. Unfortunately, LST exhibits significant diurnal variations, with temperature differences of up to 10 K or more occurring over short distances or time intervals [Li et al., 2013]. To validate our model effectively in urban settings, it would be necessary to obtain *in situ* measurements at the scale of a city and precisely at the same time as the satellite capture. Given the scale and the land cover heterogeneity of urban regions, attaining validation data in a scalable manner is extremely challenging.

Therefore, in our study, we rely on synthetic occlusions to validate our results, as described in Section 4.2.1. While this approach provides valuable insights, developing scalable *in situ* validation methods specifically tailored for ISLAND should be considered as a topic for future research. Overcoming the challenges associated with *in situ* validation would enhance the robustness and confidence of our model's performance assessment in real-world conditions.

Limitations of NLCD land cover labels: As stated in Fig. 1, our model uses the NLCD land cover data. Specifically, we use the NLCD 2019 release [Dewitz, 2021], which most accurately reflects the state of land cover labels in the year 2019. Our thermal image input, by contrast, spans from early 2017 to late 2022. Within this observational period, NLCD 2019 alone does not reflect changes in land cover due to urban expansion, meandering, or coastal erosion. NLCD refreshes every 3 years and there are versions available for 2016, 2013, etc. Although a fraction of observation dates could have potentially benefited from using the 2016 release instead of 2019, we choose not to implement multiple NLCD versions for simplicity. Despite using only the NLCD release for 2019, we still observe a significant advantage in terms of reconstructed LST when employing the NLCD dataset as input, as seen in Table 1.

Reliance of accurate cloud masks: Another assumption of our model is that all clouds are correctly labeled. Our algorithm relies on accurate cloud labeling, and errors in cloud labeling would most likely propagate to interpolated LST. Recall from Fig. 1 that both cloud and cloud shadow bitmasks are parsed from the Landsat 8 data. In Sec. 4.2.1 we showed that inaccurate cloud labels may lead to inaccurate predictions. For example, row 4 of Fig. 4 includes falsely labeled cirrus clouds, a category of clouds known to be difficult to detect [Qiu et al., 2020]. Moreover, it is difficult to reliably detect clouds in snow-covered terrain due to the spectral similarity between cloud and snow [Stillinger et al., 2019]. Finally, in some cases, we also observe that optically bright and thermally cold buildings are falsely labeled as clouds in the TIR input images, though this mislabeling is rare. The increasing prevalence of white roofing applied to increase urban albedo and decrease the UHIE may worsen the future uses of ISLAND [Fayad et al., 2021]. It is important to address these challenges and improve cloud labeling techniques to ensure the accuracy of our model's predictions.

Errors external to interpolation: As seen in Sec. 4.2.1, we present an analysis of errors introduced by the interpolator and choose not to investigate errors external to our model. Other sources of error include but are not limited to, sensor calibration, atmospheric profiles, and emissivity estimation [Li et al., 2013]. In particular, we use estimated emissivity via ASTER GED [Hulley et al., 2015], which uses optical data to temporarily adjust emissivity estimations [Cook et al., 2014]. Under cloud occlusion, the ASTER GED product likely defaults to the average value observed between 2000 - 2008 [Hulley et al., 2015], leading to increased error. Profiling and mitigating these types of errors are areas of active research [Li et al., 2013] in the field of remote sensing; such improvements are beyond the scope of this paper. We discuss potential avenues to overcome some of these constraints in Sec. 5.3.

5.2 Transferability and Scalability

We designed ISLAND to be easily accessible to the broader research community. All required inputs of our model listed in Fig. 1 are acquired from publicly available sources and are extracted from Google Earth Engine [Gorelick et al., 2017] and its Python API, geemap [Wu, 2020]. Since our model is essentially based on a set of filters, we do not require massive computing power or GPU. For context, it takes roughly 2 minutes to process one image on a 12-core CPU (AMD Ryzen 5900) with 32GB of DRAM.

Currently, our model is only available to the CONUS region, constrained by the NLCD dataset. In Sec. 5.3, we discuss potential avenues to expand the operational region.

5.3 Potential Improvements and Future Opportunities for ISLAND

Extending area of study: In Sec. 5.1, we showed that the use of the NLCD dataset currently restricts our analysis to the CONUS region. In theory, we can potentially expand to other regions as long as there are appropriate land cover labels. For example, the Copernicus CORINE Land Cover dataset [Buchhorn et al., 2020] would facilitate the extension of the model over Europe; the China land cover dataset (CLCD) [Yang and Huang, 2021] is also available, enabling research over the Asian continent. It is important to note that the performance of ISLAND is highly impacted by spatiotemporal resolution, diversity, and accuracy of land cover labels. Therefore, careful consideration should be given to the suitability and quality of the land cover datasets when expanding the study area beyond CONUS.

Incorporating Landsat 9: Our model uses Landsat 8 [USGS, 2023a] data to achieve one LST reconstruction per 16 days. Recently, the Landsat program launched a companion satellite named Landsat 9 [USGS, 2023b], carrying a nearly identical TIRS as Landsat 8. Landsat 8 and Landsat 9 are phased eight days apart. By incorporating data from both satellites, we can reduce the time gap between consecutive satellite visits to just eight days. This enables us to capture LST measurements at a higher temporal resolution.

Furthermore, Landsat 9's TIRS instrument offers some marginal improvements over Landsat 8. It features a higher radiometric resolution, with quantization increased from 12 bits to 14 bits. TIRS-2 band on Landsat 9 is better calibrated, potentially leading to higher accuracy in LST reconstruction [USGS, 2023b]. In contrast, the TIRS-2 channel on Landsat 8 has suffered from stray light issues, discouraging its usage [Ihlen, 2019]. For our algorithm, we currently utilize only the TIRS-1 channel, as depicted in Figure 1.

Incorporating deep learning: The basis of our interpolator is a set of filters designed around adjacency and temporal properties of thermal signatures. As seen in Algorithm 1 and 2, these filters are *hand crafted* to explicitly represent these relationships. While we clearly demonstrated the effectiveness of ISLAND through qualitative and quantitative analysis, we acknowledge that a well-designed deep learning algorithm has the potential to achieve even better performance. Here we highlight a few examples. Firstly, deep learning models have the capability to capture complex inter-class relationships between different land cover labels. This could enhance the overall accuracy of our interpolator. Secondly, a dynamic spatial channel that adapts based on occlusion characteristics could be incorporated, allowing the model to better handle varying cloud cover conditions. Additionally, an optimized weighting scheme, an improved cloud detection filter, and an updated NLCD land cover dataset to account for changes in land cover could be integrated into a deep learning framework. Given the complexity of the problem and the non-linear nature of LST [Wu et al., 2021], deep learning is a suitable direction for future work, but designing and training a deep learning framework might require extensive research.

5.4 Advancing Existing State-of-the-Art LST Estimates

In this paper, we showed that a large proportion of Landsat measurements are heavily degraded due to cloud contaminations. As a consequence, the actual usable temporal resolution of Landsat is much worse, falling below once per month under severe cloud occlusions. The role of ISLAND is to mitigate cloud contamination in TIR images, maximizing its usable temporal resolution.

Indeed, the addition of ISLAND represents an advance over existing methods and LST reconstructions, as shown in Fig. 9. Generally speaking, there is a trade-off between spatial resolution and temporal resolution for satellite LST products. Amongst all available satellite measurements, Landsat 8 (along with the later-launched Landsat 9) offers the best spatial resolution at 30 m, with 16-day revisit cycles. Operating in SSO, Landsat 8 has the advantage of providing global coverage and maintaining time-constant illumination conditions of the observed surfaces (except for seasonal variations). The MODIS program [Wan, 2013], consisting of a pair of satellites named Aqua and Terra, offers a much higher resolution at daily revisit cycles but provides TIR data at a much lower spatial resolution of 1 km. Satellites in geostationary orbits do provide higher temporal resolution at the expense of spatial resolution and global coverage. For example, GridSat-B1 [Knapp et al., 2011, Knapp, 2014] provides BT data at a resolution of 7792 m.

In addition to satellite-based methods, climate reanalysis data are an alternative method to obtain LST. These products are generally designed to maintain the best possible physical and temporal consistency and require prohibitive computational costs [Hakim et al., 2016]. The spatial resolution of these products is not comparable to satellite-based methods; HRRR [James et al., 2022] provides climate data at 3 km and ERA5 [Muñoz Sabater, 2019] at around 11 km. Fig. 9 provides a visual comparison of the spatial resolution of LST in ERA5 and ISLAND. Due to relatively low spatial resolution, the urban spatial structure over Philadelphia is indistinguishable in ERA5 skin temperature fields. In contrast, our method effectively removes cloud contamination and produces a high-resolution reconstruction of LST at 30 m resolution.

As shown in Sec. 4.3, many downstream applications generally benefit from increased spatial and temporal resolution. For dense urban settings, high spatial resolution is particularly desirable, making the Landsat data a preferred choice. In

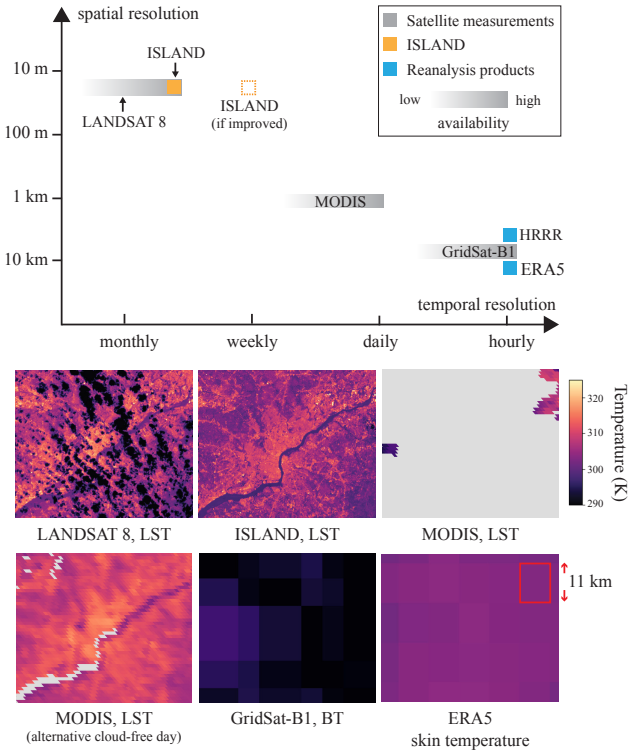

Figure 9: **Contribution in the context of spatial-temporal resolutions.** ISLAND is derived from Landsat 8, which collects LST with 16-day revisit cycles but the actual usable temporal resolution is much lower due to cloud contamination. ISLAND improves the usable temporal resolution of Landsat 8 LST data to approach its 16-day limit. If Landsat 9 data is to be integrated into a future variant of ISLAND, in theory, it could provide nearly weekly coverage (marked as if improved). Other methods provide higher temporal resolution but with substantially lower spatial resolution. The figure also displays six different LST products for Philadelphia, highlighting the spatial resolutions and the impact of cloud contamination across different methods.

Sec. 5.3, we discussed the potential of incorporating measurements from Landsat 9 to further enhance the temporal resolution to 8 days. This advancement would bring us closer to achieving consistent weekly measurements at a spatial resolution of 30 m. Such a combination of high spatial and temporal resolution of thermal measurements is instrumental to our understanding of urban areas.

5.5 Conclusions

This paper introduces ISLAND, a novel model designed to address the issue of cloud occlusion in satellite TIR images. ISLAND removes occlusion by estimating TIR pixel values through a set of spatio-temporal filters. These filters account for the land cover class, resulting in higher LST reconstruction accuracy. ISLAND addresses a fundamental limitation of TIR imaging via remote sensing, thereby dramatically increasing the number of serviceable TIR and LST images via a robust mechanism to mitigate cloud contamination. These improvements enable nearly bi-weekly coverage of LST at 30 m resolution over the CONUS region, a large advance over previously available LST products derived from remote sensing. We show ISLAND can operate in a variety of land cover types and cloud occlusion scenarios and is superior to other models tested in an ablation study. Overall, ISLAND provides a promising framework for a multitude of scientific applications that require high-resolution, frequent observations of LST, including but not limited to (1) urban heat island effects, (2) derivation of surface temperature trends, and (3) social vulnerability and urban heat stress.

Acknowledgement

The authors gratefully acknowledge the support of this research by the National Science Foundation (NSF) award numbers 1652633 and 2107313. The contributions of Pranavesh Panakkal and Jamie E. Padgett were partially supported

by NSF award number 2227467. Any opinions, findings, conclusions, or recommendations expressed in this paper are those of the authors and do not necessarily reflect the views of the sponsors.

References

Radley M Horton, Justin S Mankin, Corey Lesk, Ethan Coffel, and Colin Raymond. A review of recent advances in research on extreme heat events. *Current Climate Change Reports*, 2:242–259, 2016.

S.I. Seneviratne, X. Zhang, M. Adnan, W. Badi, C. Dereczynski, A. Di Luca, S. Ghosh, I. Iskandar, J. Kossin, S. Lewis, F. Otto, I. Pinto, M. Satoh, S.M. Vicente-Serrano, M. Wehner, and B. Zhou. *Weather and Climate Extreme Events in a Changing Climate*, page 1513–1766. Cambridge University Press, Cambridge, United Kingdom and New York, NY, USA, 2021. doi:10.1017/9781009157896.013.

José A. Sobrino, Rosa Oltra-Carrió, Guillem Sòria, Juan Carlos Jiménez-Muñoz, Belén Franch, Victoria Hidalgo, Cristian Mattar, Yves Julien, Juan Cuenca, Mireia Romaguera, J. Antonio Gómez, Eduardo De Miguel, Remo Bianchi, and Marc Paganini. Evaluation of the surface urban heat island effect in the city of madrid by thermal remote sensing. 34(9):3177–3192, 2013. ISSN 0143-1161. doi:10.1080/01431161.2012.716548. URL https://doi.org/10.1080/01431161.2012.716548. Publisher: Taylor & Francis _eprint: https://doi.org/10.1080/01431161.2012.716548.

Xin Huang and Ying Wang. Investigating the effects of 3d urban morphology on the surface urban heat island effect in urban functional zones by using high-resolution remote sensing data: A case study of wuhan, central china. 152: 119–131, 2019. ISSN 0924-2716. doi:10.1016/j.isprsjprs.2019.04.010. URL https://www.sciencedirect.com/science/article/pii/S0924271619301066.

Filoteo Gomez-Martinez, Kirsten M. de Beurs, Jennifer Koch, and Jeffrey Widener. Multi-temporal land surface temperature and vegetation greenness in urban green spaces of puebla, mexico. 10(2):155, 2021. ISSN 2073-445X. doi:10.3390/land10020155. URL https://www.mdpi.com/2073-445X/10/2/155.

I. R. Orimoloye, S. P. Mazinyo, W. Nel, and A. M. Kalumba. Spatiotemporal monitoring of land surface temperature and estimated radiation using remote sensing: human health implications for east london, south africa. *Environmental Earth Sciences*, 77(3):77, Jan 2018. ISSN 1866-6299. doi:10.1007/s12665-018-7252-6. URL https://doi.org/10.1007/s12665-018-7252-6.

Sylvia G Dee, Ebrahim Nabizadeh, Christine L Nittrouer, Jane W Baldwin, Chelsea Li, Lizzy Gaviria, Selena Guo, Karen Lu, Beck Miguel Saunders-Shultz, Emily Gurwitz, et al. Increasing health risks during outdoor sports due to climate change in texas: Projections versus attitudes. *GeoHealth*, 6(8):e2022GH000595, 2022.

Zhao-Liang Li, Bo-Hui Tang, Hua Wu, Huazhong Ren, Guangjian Yan, Zhengming Wan, Isabel F. Trigo, and José A. Sobrino. Satellite-derived land surface temperature: Current status and perspectives. 131:14–37, 2013. ISSN 0034-4257. doi:10.1016/j.rse.2012.12.008. URL https://www.sciencedirect.com/science/article/pii/S0034425712004749.

USGS. Landsat-8 image courtesy of the u.s. geological survey, 2023a. URL https://www.usgs.gov/landsat-missions/landsat-8. Accessed: April 3, 2023.

USGS. Landsat-9 image courtesy of the u.s. geological survey, 2023b. URL https://www.usgs.gov/landsat-missions/landsat-9. Accessed: April 3, 2023.

David R Streutker. Satellite-measured growth of the urban heat island of houston, texas. 85(3):282–289, 2003. ISSN 0034-4257. doi:10.1016/S0034-4257(03)00007-5. URL https://www.sciencedirect.com/science/article/pii/S0034425703000075.

Vahid Eisavi, Ahmad Maleknezhad Yazdi, and Seyeed Ali Niknezhad. Spatial and temporal modeling of wetland surface temperature using landsat-8 imageries in sulduz, iran. *Journal of the Faculty of Forestry Istanbul University*, 66(1): 46–58, Jan 2016. ISSN 0535-8418, 1309-6257. doi:10.17099/jffiu.26733. URL https://dergipark.org.tr/en/pub/jffiu/issue/18906/198876.

Quentin Demarquet, Sébastien Rapinel, Simon Dufour, and Laurence Hubert-Moy. Long-term wetland monitoring using the landsat archive: A review. *Remote Sensing*, 15(3):820, Jan 2023. ISSN 2072-4292. doi:10.3390/rs15030820. URL https://www.mdpi.com/2072-4292/15/3/820.

Zhonghai Jin, Yuanchong Zhang, Anthony Del Genio, Gavin Schmidt, and Maxwell Kelley. Cloud scattering impact on thermal radiative transfer and global longwave radiation. *Journal of quantitative spectroscopy & radiative transfer*, 239:106669, Dec 2019. ISSN 0022-4073. doi:10.1016/j.jqsrt.2019.106669. URL https://www.ncbi.nlm.nih.gov/pmc/articles/PMC7351100/.

David P. Roy, Junchang Ju, Philip Lewis, Crystal Schaaf, Feng Gao, Matt Hansen, and Erik Lindquist. Multi-temporal modis–landsat data fusion for relative radiometric normalization, gap filling, and prediction of landsat data. *Remote Sensing of Environment*, 112(6):3112–3130, Jun 2008. ISSN 0034-4257. doi:10.1016/j.rse.2008.03.009. URL https://www.sciencedirect.com/science/article/pii/S0034425708001065.

Thuy Trang Vo, Leiqiu Hu, Lulin Xue, Qi Li, and Sisi Chen. Urban effects on local cloud patterns. *Proceedings of the National Academy of Sciences*, 120(21):e2216765120, 2023.

NOAA. Comparative climatic data, 2020. URL https://www.ncei.noaa.gov/products/land-based-station/comparative-climatic-data.

W. R. Tobler. A computer movie simulating urban growth in the detroit region. *Economic Geography*, 46:234–240, 1970. ISSN 0013-0095. doi:10.2307/143141. URL https://www.jstor.org/stable/143141.

Gargi Chaudhuri and Niti B. Mishra. Spatio-temporal dynamics of land cover and land surface temperature in ganges-brahmaputra delta: A comparative analysis between india and bangladesh. *Applied Geography*, 68:68–83, Mar 2016. ISSN 0143-6228. doi:10.1016/j.apgeog.2016.01.002. URL https://www.sciencedirect.com/science/article/pii/S0143622816300029.

Jiacheng Zhao, Xiang Zhao, Shunlin Liang, Tao Zhou, Xiaozheng Du, Peipei Xu, and Donghai Wu. Assessing the thermal contributions of urban land cover types. *Landscape and Urban Planning*, 204:103927, Dec 2020. ISSN 0169-2046. doi:10.1016/j.landurbplan.2020.103927. URL https://www.sciencedirect.com/science/article/pii/S0169204619311971.

H. M. Imran, Anwar Hossain, A. K. M. Saiful Islam, Ataur Rahman, Md Abul Ehsan Bhuiyan, Supria Paul, and Akramul Alam. Impact of land cover changes on land surface temperature and human thermal comfort in dhaka city of bangladesh. *Earth Systems and Environment*, 5(3):667–693, Sep 2021. ISSN 2509-9434. doi:10.1007/s41748-021-00243-4. URL https://doi.org/10.1007/s41748-021-00243-4.

Limin Yang, Suming Jin, Patrick Danielson, Collin Homer, Leila Gass, Stacie M. Bender, Adam Case, Catherine Costello, Jon Dewitz, Joyce Fry, Michelle Funk, Brian Granneman, Greg C. Liknes, Matthew Rigge, and George Xian. A new generation of the united states national land cover database: Requirements, research priorities, design, and implementation strategies. 146:108–123, 2018. ISSN 09242716. doi:10.1016/j.isprsjprs.2018.09.006. URL https://linkinghub.elsevier.com/retrieve/pii/S092427161830251X.

Noel Gorelick, Matt Hancher, Mike Dixon, Simon Ilyushchenko, David Thau, and Rebecca Moore. Google earth engine: Planetary-scale geospatial analysis for everyone. *Remote Sensing of Environment*, 2017. doi:10.1016/j.rse.2017.06.031. URL https://doi.org/10.1016/j.rse.2017.06.031.

Xiaolin Zhu, Feng Gao, Desheng Liu, and Jin Chen. A modified neighborhood similar pixel interpolator approach for removing thick clouds in landsat images. *IEEE Geoscience and Remote Sensing Letters*, 9(3):521–525, 2011.

Ruyin Cao, Yang Chen, Jin Chen, Xiaolin Zhu, and Miaogen Shen. Thick cloud removal in landsat images based on autoregression of landsat time-series data. 249:112001, 2020. ISSN 0034-4257. doi:10.1016/j.rse.2020.112001. URL https://www.sciencedirect.com/science/article/pii/S0034425720303710.

Álvaro Moreno-Martínez, Emma Izquierdo-Verdiguier, Marco P. Maneta, Gustau Camps-Valls, Nathaniel Robinson, Jordi Muñoz-Marí, Fernando Sedano, Nicholas Clinton, and Steven W. Running. Multispectral high resolution sensor fusion for smoothing and gap-filling in the cloud. 247:111901, 2020. ISSN 0034-4257. doi:10.1016/j.rse.2020.111901. URL https://www.sciencedirect.com/science/article/pii/S0034425720302716.

Zhengming Wan. Modis land surface temperature products. Dec 2013. URL https://lpdaac.usgs.gov/documents/118/MOD11_User_Guide_V6.pdf.

Penghai Wu, Zhixiang Yin, Chao Zeng, Si-Bo Duan, Frank-Michael Göttsche, Xiaoshuang Ma, Xinghua Li, Hui Yang, and Huanfeng Shen. Spatially continuous and high-resolution land surface temperature product generation: A review of reconstruction and spatiotemporal fusion techniques. *IEEE Geoscience and Remote Sensing Magazine*, 9(3):112–137, Sep 2021. ISSN 2168-6831. doi:10.1109/MGRS.2021.3050782.

Wenping Yu, Junlei Tan, Mingguo Ma, Xiaolu Li, Xiaojun She, and Zengjing Song. An effective similar-pixel reconstruction of the high-frequency cloud-covered areas of southwest china. *Remote Sensing*, 11(3), 2019. ISSN 2072-4292. doi:10.3390/rs11030336. URL https://www.mdpi.com/2072-4292/11/3/336.

Chao Zeng, Huanfeng Shen, Mingliang Zhong, Liangpei Zhang, and Penghai Wu. Reconstructing modis lst based on multitemporal classification and robust regression. *IEEE Geoscience and Remote Sensing Letters*, 12(3):512–516, 2015. doi:10.1109/LGRS.2014.2348651.

Xiaolin Zhu, Si-Bo Duan, Zhao-Liang Li, Penghai Wu, Hua Wu, Wei Zhao, and Yonggang Qian. Reconstruction of land surface temperature under cloudy conditions from landsat 8 data using annual temperature cycle model. *Remote Sensing of Environment*, 281:113261, 2022. ISSN 0034-4257. doi:https://doi.org/10.1016/j.rse.2022.113261. URL https://www.sciencedirect.com/science/article/pii/S0034425722003674.

J. A. Augustine, J. J. DeLuisi, and C. N. Long. Surfrad - a national surface radiation budget network for atmospheric research. *Bulletin of the American Meteorological Society*, 81(10):2341–2357, 2000. URL www.scopus.com.

Vaughn Ihlen. *Landsat 8 (L8) Data Users Handbook*. Nov 2019.

Gyanesh Chander, Brian L. Markham, and Dennis L. Helder. Summary of current radiometric calibration coefficients for landsat mss, tm, etm+, and eo-1 ali sensors. *Remote Sensing of Environment*, 113(5):893–903, May 2009. ISSN 0034-4257. doi:10.1016/j.rse.2009.01.007. URL https://www.sciencedirect.com/science/article/pii/S0034425709000169.

Jon Dewitz. National land cover database (NLCD) 2019 products, 2021. URL https://www.sciencebase.gov/catalog/item/5f21cef582cef313ed940043. Type: dataset.

Qiusheng Wu. geemap: A python package for interactive mapping with google earth engine. *Journal of Open Source Software*, 5(51):2305, Jul 2020. ISSN 2475-9066. doi:10.21105/joss.02305. URL https://joss.theoj.org/papers/10.21105/joss.02305.

Sylvain Paris, Pierre Kornprobst, Jack Tumblin, Frédo Durand, et al. Bilateral filtering: Theory and applications. *Foundations and Trends® in Computer Graphics and Vision*, 4(1):1–73, 2009.

Glynn C. Hulley, Simon J. Hook, Elsa Abbott, Nabin Malakar, Tanvir Islam, and Michael Abrams. The ASTER global emissivity dataset (ASTER GED): Mapping earth's emissivity at 100 meter spatial scale. 42(19):7966–7976, 2015. ISSN 1944-8007. doi:10.1002/2015GL065564. URL https://onlinelibrary.wiley.com/doi/abs/10.1002/2015GL065564.

Monica Cook, John R. Schott, John Mandel, and Nina Raqueno. Development of an operational calibration methodology for the landsat thermal data archive and initial testing of the atmospheric compensation component of a land surface temperature (lst) product from the archive. *Remote Sensing*, 6(1111):11244–11266, Nov 2014. ISSN 2072-4292. doi:10.3390/rs61111244. URL https://www.mdpi.com/2072-4292/6/11/11244.

United States Census Bureau. City and town population totals: 2020-2021, 2023. URL https://www.census.gov/data/tables/time-series/demo/popest/2020s-total-cities-and-towns.html.

Ellen M Rathje, Clint Dawson, Jamie E Padgett, Jean-Paul Pinelli, Dan Stanzione, Ashley Adair, Pedro Arduino, Scott J Brandenberg, Tim Cockerill, Charlie Dey, et al. Designsafe: New cyberinfrastructure for natural hazards engineering. *Natural Hazards Review*, 18(3):06017001, 2017.

Yuhao Liu, Pranavesh Panakkal, Sylvia Dee, Guha Balakrishnan, Jamie Padgett, and Ashok Veeraraghavan. Island: Informing brightness and surface temperature through a land cover based interpolator, 2023. URL https://www.designsafe-ci.org/data/browser/public/designsafe.storage.published/PRJ-3938.

Valerio Baiocchi, Fabio Zottele, and Donatella Dominici. Remote sensing of urban microclimate change in l'aquila city (italy) after post-earthquake depopulation in an open source GIS environment. 17, 2017. doi:10.3390/s17020404.

V. Moller, R. van Diemen, J.B.R. Matthews, C. Méndez, S. Semenov, J.S. Fuglestvedt, and A. Reisinger. Annex ii: Glossary. In H.-O. Pörtner, D.C. Roberts, M. Tignor, E.S. Poloczanska, K. Mintenbeck, A. Alegría, M. Craig, S. Langsdorf, S. Löschke, V. Möller, A. Okem, and B. Rama, editors, *Climate Change 2022: Impacts, Adaptation and Vulnerability. Contribution of Working Group II to the Sixth Assessment Report of the Intergovernmental Panel on Climate Change*, pages 2897–2930. Cambridge University Press, Cambridge, UK and New York, NY, USA, 2022. doi:10.1017/9781009325844.029.

Lans P Rothfusz and NWS Southern Region Headquarters. The heat index equation (or, more than you ever wanted to know about heat index). *Fort Worth, Texas: National Oceanic and Atmospheric Administration, National Weather Service, Office of Meteorology*, 9023:640, 1990.

The White House. Justice40 Initiative | Environmental Justice | The White House — whitehouse.gov. https://www.whitehouse.gov/environmentaljustice/justice40/, 2022. [Accessed 22-May-2023].

Centers for Disease Control, Prevention and ATSDR, Analysis and Services Program, and Agency for Toxic Substances and Disease Registry/ Geospatial Research. CDC/ATSDR Social Vulnerability Index 2020 Database US, 2020. URL https://www.atsdr.cdc.gov/placeandhealth/svi/data_documentation_download.html.

Caitlín Mc Shane, Johannes H Uhl, and Stefan Leyk. Gridded land use data for the conterminous united states 1940–2015. *Scientific Data*, 9(1):493, 2022.

USGS, 2019. URL https://www.usgs.gov/special-topics/water-science-school/science/condensation-and-water-cycle.

William R. Cotton, George Bryan, and Susan C. van den Heever. *Chapter 7 - Cumulus Clouds*, volume 99 of *Storm and Cloud Dynamics*, page 243–314. Academic Press, Jan 2011. doi:10.1016/S0074-6142(10)09913-4. URL https://www.sciencedirect.com/science/article/pii/S0074614210099134.

L. Boldt-Christmas. Polar and sun-synchronous orbit, 2020. URL https://www.esa.int/ESA_Multimedia/Images/2020/03/Polar_and_Sun-synchronous_orbit.

Shi Qiu, Zhe Zhu, and Curtis E. Woodcock. Cirrus clouds that adversely affect landsat 8 images: What are they and how to detect them? *Remote Sensing of Environment*, 246:111884, Sep 2020. ISSN 0034-4257. doi:10.1016/j.rse.2020.111884. URL https://www.sciencedirect.com/science/article/pii/S0034425720302546.

Timbo Stillinger, Dar A. Roberts, Natalie M. Collar, and Jeff Dozier. Cloud masking for landsat 8 and modis terra over snow-covered terrain: Error analysis and spectral similarity between snow and cloud. *Water Resources Research*, 55(7):6169–6184, Jul 2019. ISSN 0043-1397, 1944-7973. doi:10.1029/2019WR024932. URL https://onlinelibrary.wiley.com/doi/10.1029/2019WR024932.

Fadye Al Fayad, Wahid Maref, and Mohamed M. Awad. Review of white roofing materials and emerging economies with focus on energy performance cost-benefit, maintenance, and consumer indifference. *Sustainability*, 13(17):9967, Jan 2021. ISSN 2071-1050. doi:10.3390/su13179967. URL https://www.mdpi.com/2071-1050/13/17/9967.

Marcel Buchhorn, Myroslava Lesiv, Nandin-Erdene Tsendbazar, Martin Herold, Luc Bertels, and Bruno Smets. Copernicus global land cover layers—collection 2. *Remote Sensing*, 12(6):1044, Jan 2020. ISSN 2072-4292. doi:10.3390/rs12061044. URL https://www.mdpi.com/2072-4292/12/6/1044.

Jie Yang and Xin Huang. The 30m annual land cover dataset and its dynamics in china from 1990 to 2019. *Earth System Science Data*, 13(8):3907–3925, Aug 2021. ISSN 1866-3508. doi:10.5194/essd-13-3907-2021. URL https://essd.copernicus.org/articles/13/3907/2021/.

Kenneth R. Knapp, Steve Ansari, Caroline L. Bain, Mark A. Bourassa, Michael J. Dickinson, Chris Funk, Chip N. Helms, Christopher C. Hennon, Christopher D. Holmes, George J. Huffman, James P. Kossin, Hai-Tien Lee, Alexander Loew, and Gudrun Magnusdottir. Globally gridded satellite observations for climate studies. *Bulletin of the American Meteorological Society*, 92(7):893–907, Jul 2011. ISSN 0003-0007, 1520-0477. doi:10.1175/2011BAMS3039.1. URL https://journals.ametsoc.org/doi/10.1175/2011BAMS3039.1.

NOAA CDR Program Knapp, Kenneth R. Noaa climate data record (cdr) of intersatellite calibrated gridded satellite data from isccp b1 (gridsat-b1) 11 micron brightness temperature, version 2, 2014. URL https://data.nodc.noaa.gov/cgi-bin/iso?id=gov.noaa.ncdc:C00829.

Gregory J. Hakim, Julien Emile-Geay, Eric J. Steig, David Noone, David M. Anderson, Robert Tardif, Nathan Steiger, and Walter A. Perkins. The last millennium climate reanalysis project: Framework and first results. *Journal of Geophysical Research: Atmospheres*, 121(12):6745–6764, Jun 2016. ISSN 2169-897X, 2169-8996. doi:10.1002/2016JD024751. URL https://onlinelibrary.wiley.com/doi/10.1002/2016JD024751.

Eric P James, Curtis R Alexander, David C Dowell, Stephen S Weygandt, Stanley G Benjamin, Geoffrey S Manikin, John M Brown, Joseph B Olson, Ming Hu, Tatiana G Smirnova, et al. The high-resolution rapid refresh (hrrr): An hourly updating convection-allowing forecast model. part ii: Forecast performance. *Weather and Forecasting*, 37(8): 1397–1417, 2022.

J. Muñoz Sabater. Era5-land monthly averaged data from 2001 to present, 2019. URL https://cds.climate.copernicus.eu/doi/10.24381/cds.68d2bb30.